

Integrated diagenetic and sequence stratigraphy of a late Oligocene–early Miocene, mixed-sediment platform (Austral Basin, southern Patagonia): Resolving base-level and paleoceanographic changes, and paleoaquifer characteristics

George R. Dix ^{a,b,*}, Ana Parras ^c

^a Ottawa-Carleton Geoscience Centre, Canada

^b Department of Earth Sciences, Carleton University, 2160 Herzberg Laboratories, Ottawa, Ontario K1S 5B6, Canada

^c INCITAP (CONICET-UNLPam), Facultad de Ciencias Exactas y Naturales, Universidad Nacional de La Pampa, Uruguay 151, 6300 Santa Rosa, La Pampa, Argentina

ARTICLE INFO

Article history:

Received 20 December 2013

Received in revised form 15 April 2014

Accepted 15 April 2014

Available online 26 April 2014

Editor: B. Jones

Keywords:

Marine and burial diagenesis

Sequence stratigraphy

Mixed sediment

Oligocene–Miocene

Austral Basin

ABSTRACT

A condensed (~20-m-thick) marine transgressive-highstand succession comprises the upper San Julián Formation (upper Oligocene–lower Miocene) of the northern retroarc Austral Basin, southern Patagonia. Mixed-sediment facies identify a shelf-interior setting, part of an overall warm-temperate regional platform of moderate energy. Giant oyster-dominated skeletal–hiatal accumulations along the maximum flooding surface and forming high-energy event beds in the highstand succession preserve relict micrite in protected shelter porosity, and identify periods of reduced sediment accumulation. The stratigraphic distribution of marine-derived glaucony and diagenetic carbonates is spatially related to sequence development. Depositional siderite coincides with prominent marine transgression, defining transient mixing of marine and meteoric waters across coastal-plain deposits. Chemically evolved autochthonous glaucony coincides with periods of extended seafloor exposure and transgressions that bracket the marine succession, and within the oyster-dominated skeletal accumulations. Seafloor cement, likely once magnesian calcite, formed in association with an encrusting/boring biota along the maximum flooding surface in concert with incursion of cool (11–13 °C) water. The cement is present locally in skeletal event beds in the highstand succession suggesting a possible association with high-order base-level change and cooler water. As the highstand succession coincides with elevated global sea level in the late Oligocene–early Miocene, the locally marine-cemented glauconitic skeletal event beds in the highstand succession may identify higher order glacio-eustatic control. Local stratal condensation, however, is best explained by regional differences in basement subsidence. In the burial realm, carbonate diagenesis produced layers of phreatic calcrete coincident with skeletal-rich deposits. Zeolite (clinoptilolite-K) cement is restricted to the lowermost marine transgressive interval probably due to initial elevated metastability of reworked weathered silicates. Clay (illite)-cement is restricted to siliciclastic-rich intervals wherein skeletal carbonate did not buffer pore-water pH. Diagenetic carbonate geochemistry (Sr, Na, and $\delta^{18}\text{O}$ and $\delta^{13}\text{C}$) shows that, with burial, the transgressive and highstand system tracts developed as distinct paleoaquifers resulting from different proximities to meteoric recharge zones.

© 2014 Elsevier B.V. All rights reserved.

1. Introduction

The San Julián Formation is a mixed-sediment (siliciclastic, volcanoclastic, glaucony, skeletal carbonate) succession of late Oligocene–early Miocene age, representing a shelf-interior setting in the northern retroarc foreland of the Austral Basin, southern Patagonia (Fig. 1). The unit represents the first of two regional transgressions across the Atlantic margin through to the early Miocene (Malumíán and Nánuez, 2011). In this formation, authigenic silicates and calcite textures related

to marine and burial diagenesis are differentially distributed within a transgressive-highstand system tract succession. Stratigraphically constrained diagenesis in siliciclastic, mixed sediment, and carbonate depositional sequences (e.g., Amorosi, 1995; Tucker, 1993; Taylor et al., 2000; Morad et al., 2012) is expected because controls on marine diagenesis (base level, sediment accumulation, oceanography) influence geometry, stratigraphy, and facies of depositional sequences (Handford and Loucks, 1993; Catuneanu, 2006); and, these, in turn, along with base level, influence flowpaths and characteristics of burial pore fluids. For the San Julián Formation, integration of diagenetic and sequence stratigraphy produces two outcomes that are applicable to other geologic settings. First, we demonstrate that this approach offers a sensitive measure of changes in base level and related paleoceanography. This allows

* Corresponding author at: Department of Earth Sciences, Carleton University, Ottawa, Ontario, K1S 5B6, Canada. Tel.: +1 569 7877 1302; fax: +1 613 520 5613.

E-mail address: george.dix@carleton.ca (G.R. Dix).

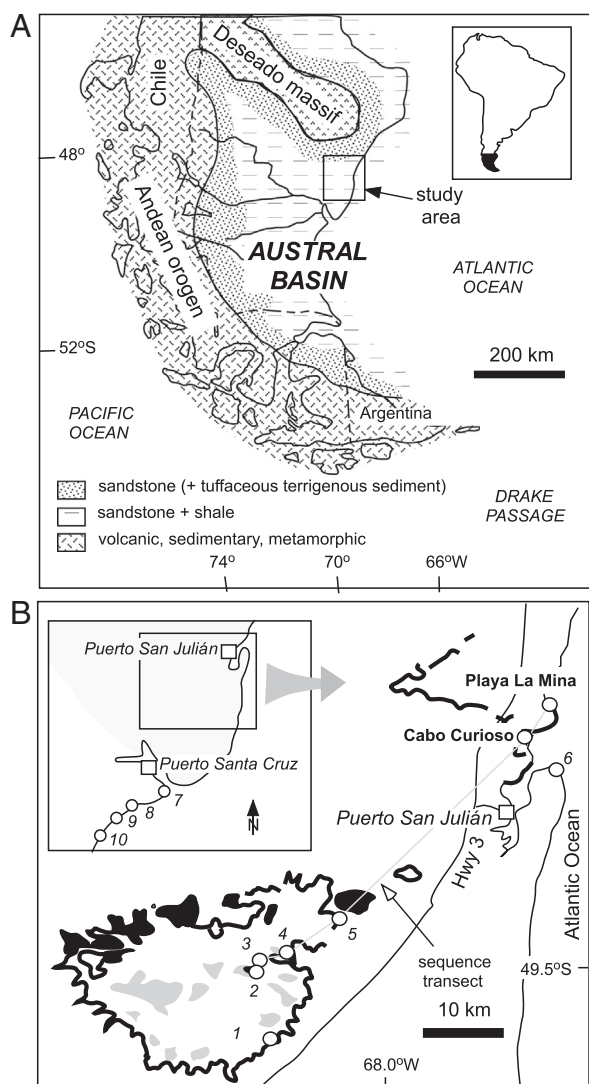


Fig. 1. A) Study area (box outline: panel B) shown relative to early Miocene maximum transgression of the Austral Basin, southern Patagonia (Malumián and Náñez, 2011). The Deseado Massif is underlain by Proterozoic through Cenozoic rocks (Guido et al., 2004), and the curved Andean orogen reflects post-Paleozoic evolution of the Nazca–South American plate boundary (Suárez et al., 2000) and Paleogene opening of the Drake Passage (Scher and Martin, 2006). B) Outcrop pattern (thick black line) of the San Julián Formation (Parras and Casadío, 2005) with location of coastal sections, Cabo Curioso and Playa La Mina. Numbered localities are referred to in Fig. 3A and Fig. 13C, with geographic coordinates provided in Table 1. The shaded area in the inset map shows the present-day exposed and burial limits of the Deseado Massif (Guido et al., 2004).

the evaluation of potential external drivers that, during the Oligocene–Miocene, included global sea level (Kominz et al., 2008) and related glaciations in Antarctica (Webb and Strong, 2006); changes in Southern Ocean paleoceanography related to plate tectonics (Scher and Martin, 2006); and Andean orogenesis (Suárez et al., 2000; Thomson et al., 2001). A second outcome of integrated analysis is that sequence architecture delimits the burial geometry of geochemically distinct paleoaquifers contained within a host depositional sequence.

2. Geologic setting

2.1. Regional geology

The Austral Basin is underlain by an upper Jurassic through Quaternary sedimentary succession that thickens (<8 km) toward the Andean

orogen (Russo et al., 1980). The arc of the southern Andean orogen (Fig. 1A) records, in part, development of the Patagonian fold-and-thrust belt that began by the latest Cretaceous or early Paleogene, and transformed the basin from an early Mesozoic backarc basin to a retroarc foreland basin (Suárez et al., 2000). From the late Cretaceous through the late Miocene, progressive eastward migration of retroarc deformation resulted in uplift and volcanic-arc expansion (Thomson et al., 2001; Folguera and Ramos, 2011).

The study area lies in the northern Austral Basin (Fig. 1A). In this region, upper Paleogene–lower Neogene stratigraphy characterizes two periods of regional transgressions, then basin-fill leading to continental deposition (Fig. 2). Continental and coal-bearing coastal-plain siliciclastics of the Oligocene Río Leona Formation, that lies to the west and south of the study area, accumulated under cool conditions in the early late Oligocene (Barreda et al., 2009). In the study area, the transgressive San Julián Formation onlaps felsic volcanics and siliciclastics of the Jurassic Bahía Laura Group (Parras and Casadío, 2005) that form part of a basement complex represented by the Deseado Massif (Fig. 1; Guido et al., 2004). The formation contains a mixed-sediment depositional sequence of late Oligocene (Chattian) through early Miocene age (Fig. 2). It documents the establishment of a warm-temperate shelf-interior setting (Parras and Casadío, 2005; Erdmann et al., 2008) coincident with global warming in the late Oligocene (Zachos et al., 2001). The San Julián–Monte León Formation contact was interpreted to be unconformable (Fig. 2) based on microfaunal succession (Náñez et al., 2009), and marks renewed regional transgression in the early Miocene that established widespread open-shelf conditions dominated by fine-grained open-shelf siliciclastics, with coarser coastal facies marginal to the orogen (Fig. 1A). Transgression coincided with significant incursion of cold Southern Ocean water across the Atlantic margin (Malumián and Náñez, 2011). By the middle Miocene, continued orogenic uplift led to increased aridity (Iglesias et al., 2011) and basin-fill such that the once marine basin became an arid continental landscape underlain by the siliciclastic Santa Cruz Formation (Fig. 2; Fleagle et al., 1995; Matheos and Raigemborn, 2012).

2.2. The San Julián Formation

The formation is well stratified, its mixed sediment represented mostly by volcanic-derived siliciclastics, glaucony, and skeletal carbonate. A sinuous outcrop pattern (Fig. 1B) characterizes exposures in escarpments along the coast and inland within the Gran Bajo de San Julián. The formation contains two members (Fig. 2). The Gran Bajo

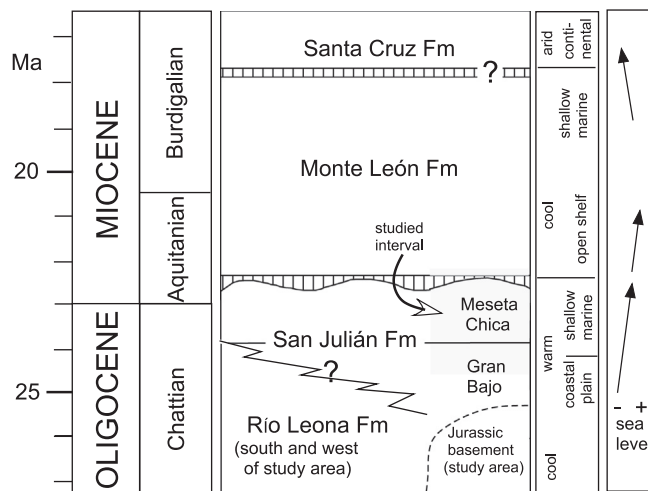


Fig. 2. Upper Oligocene–lower Miocene regional stratigraphy, depositional environments, and paleoclimatic information (Parras et al., 2008; Barreda et al., 2009; Náñez et al., 2009; Malumián and Náñez, 2011; Parras et al., 2012) with timescale of Gradstein et al. (2012).

Member has a lower succession of thin-bedded coal, fine-grained muddy to sandy siliciclastics, and oyster-bearing mixed sediment that represent marginal-marine coastal plain deposits (Parras and Casadío, 2005). The upper part of the member, and the overlying Meseta Chica Member (Fig. 2), consist of shallow-marine skeletal-rich mixed sediment with prominent beds of oyster-rich (*Crassostrea? hatcheri*) skeletal rudstone (Bertels, 1970; Parras and Casadío, 2005; Nández et al., 2009).

The formation contains a transgressive-highstand system tract succession (Fig. 3A; Parras and Casadío, 2005). Above a regional marine ravinement surface within the transgressive system tract, the marine succession thins over ~30 km from ~50 m in the large interior Gran Bajo depression to ~20 m at two coastal exposure (Fig. 3A), Cabo Curioso and Playa La Mina (Fig. 1B). The transgressive system tract coincides with both coastal-plain and marine deposits of the Gran Bajo Member (Fig. 3A), wherein regional marine ravinement defines a significant erosional paleosurface related to transgression. The maximum flooding surface coincides with the Gran Bajo–Meseta Chica member boundary (Fig. 3A); and, the top of the highstand succession coincides with the San Julián–Monte León formation boundary. Sr-isotope data (Fig. 3B; Parras et al., 2012) indicates that the duration of highstand deposition (~22.5 to ~23.5 Ma) fits within a global sea level highstand spanning the Oligocene–Miocene boundary (Fig. 3B).

3. Methodology

Two coastal sections, Cabo Curioso and Playa La Mina (Fig. 1B; Table 1), offer excellent exposure and easy access. Lithologically, they are representative of the San Julián Formation regionally (Manassero et al., 1997; Parras and Casadío, 2005). Our rock classification scheme incorporates Mount's (1984) system for mixed sediment modified with carbonate textural attributes (Embry and Klován, 1971) and silicate mineralogy (Dott, 1964). Field-based determination of lithologies was supported by thin-section petrography and carbonate cathodoluminescence microscopy (ELM-2 Luminoscope: 50 mTorr and 12 kV) using polished thin sections. Clay mineralogy was determined by powder X-ray (Cu) diffractometry (Carleton University): the clay fraction was extracted by rock disaggregation in distilled water, concentrated using a centrifuge, then air-dried on a glass slide. Texture and fabric of clay cement were examined using a Tescan Vega-II XMU VPSEM with an Oxford Inca Energy 250X EDS (Carleton University).

Trace element geochemistry was determined using a Camebax MBX electron microprobe and wavelength (WDX) spectrometry (Carleton University). Detection limits for oxides are ~100 ppm. Stable (C, O) isotope analysis was carried out at the Queen's Facility for Isotope Research (Queen's University, Canada). Carbonate powders were obtained first by spot microdrilling, then washed in deionized water three times and

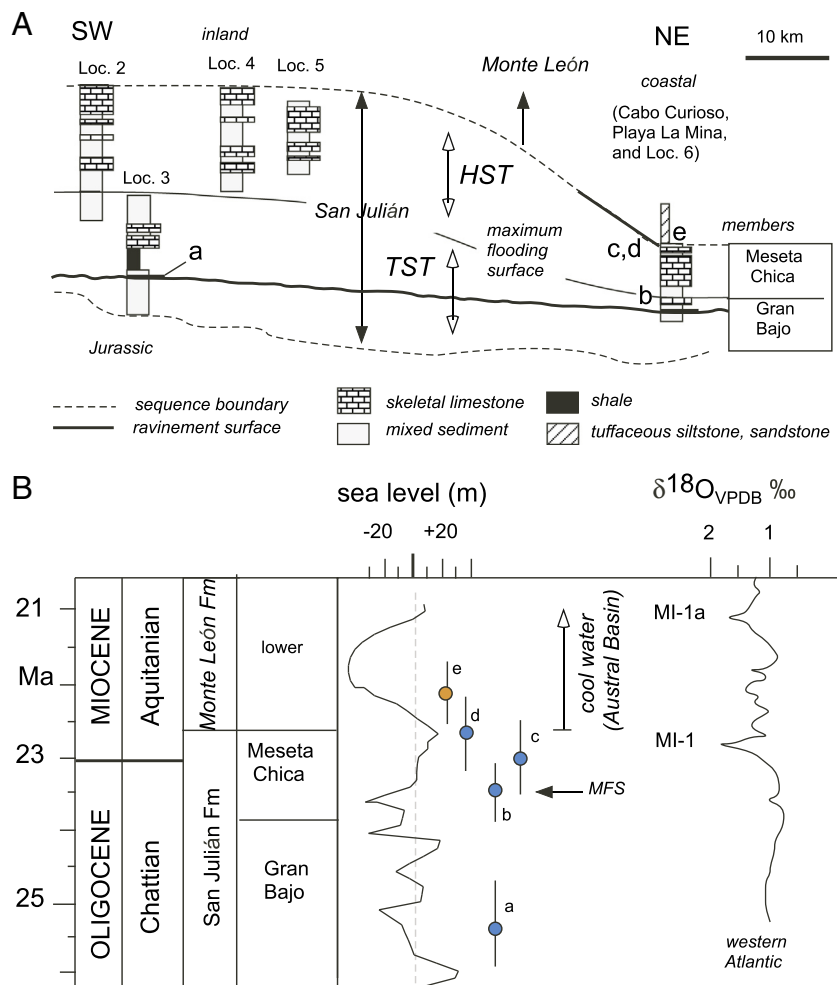


Fig. 3. (A) Sequence stratigraphic architecture of the San Julián Formation (Parras and Casadío, 2005; this study), with locality numbers as noted in Table 1. Letters a–e identify stratigraphic positions of Sr-isotope age dates tied to panel B. (B) Sr-isotope mean values (circles) and standard error (lines) from Parras et al. (2012); their Table 3, last two columns) are from stratigraphic positions (a–e) identified in panel A, and shown relative to the global sea level curve (Kominz et al., 2008) tuned to the timescale of Gradstein et al. (2012; see <http://geology.rutgers.edu/people/faculty/242-kenneth-g-miller>, columns G and H in data table). The δ¹⁸O curve is based on planktonic foraminifers from Site 929 (Ocean Drilling Program) in the western equatorial Atlantic, and identify glacial maxima, M1 and M1-1a (Paul et al., 2000).

Table 1
Section location coordinates.

Locality ^a	This study	Parras et al. (2012)	Latitude	Longitude	Reference
Meseta Chica	2	MC	49° 31' 00.0" S	68° 15' 00.0" W	1
Gran Bajo	3	GB	49° 30' 46.0" S	68° 14' 00.0" W	1, 2
La Colmena	5	LC	49° 27' 01.0" S	68° 04' 46.0" W	1, 2
Cabo Curioso		CC	49° 13' 08.0" S	67° 40' 20.0" W	1, 2
Sección 5	4	S5	49° 29' 49.0" S	68° 11' 30.0" W	1
Nido de Águila	1	NA	49° 36' 16.0" S	68° 13' 50.0" W	1, 2
Punta Asconapé	6	PA	49° 14' 56.2" S	67° 36' 49.2" W	4
Playa La Mina		PLM	49° 09' 24.0" S	67° 38' 04.0" W	4
Darwin Section	7	DS	50° 07' 40.0" S	68° 24' 10.0" W	3
Restinga Norte	8	RN	50° 19' 31.7" S	68° 52' 00.3" W	4
Cabeza de León	9	CL	50° 21' 25.4" S	68° 53' 05.9" W	4
Las Cuevas	10	CML	50° 22' 59.1" S	68° 55' 34.5" W	4

^a Numbered localities (this study) are shown in Figs. 1B, 3A; locality to abbreviations are from Parras et al. (2012); references (1–4) are as follows: 1, Parras and Casadío (2005, 2006); 2, Parras et al. (2008); 3, Parras and Griffin (2009); 4, Parras et al. (2012).

dried. $\delta^{18}\text{O}$ (VSMOW) and $\delta^{13}\text{C}$ (VPDB) were measured from CO_2 released through sample dissolution (0.5 mg) in 100% H_3PO_4 following 4 h of reaction at 72 °C in a ThermoFinnigan GasBench in-line with a Delta-XL mass spectrometer. Replicate analyses and comparisons with laboratory standards are within 0.2‰ for both $\delta^{18}\text{O}$ and $\delta^{13}\text{C}$ values. Fractionation factors for oxygen are from O'Neil et al. (1969), and for carbon from Deines et al. (1974). We recalculated VSMOW data to the VPDB reference.

4. Sequence lithostratigraphic patterns, San Julián Formation

From sedimentary attributes recorded at each section (Fig. 4), we describe facies successions across key stratigraphic boundaries; facies

attributes of skeletal rudstones; and, grain types that constitute the siliciclastic component throughout the sections. Overall, the highstand succession is visually prominent with a brownish orange color compared to the overlying Monte León Formation (Fig. 5A) and underlying, mostly gray, transgressive systems tract.

4.1. Ravinement surface, Gran Bajo Member

The marine ravinement surface (Fig. 3A) is well exposed at both sections (Fig. 4). It is a strongly burrowed disconformity (Fig. 5B) with a *Glossifungites* assemblage (sensu Parras and Casadío, 2005). The paleosurface caps a thinly bedded, coal-bearing, succession of non-calcareous siltstone and fine-grained lithic arenite with herringbone cross-stratification (Fig. 4).

At Cabo Curioso, the disconformity is overlain by a ~40-cm-thick, skeletal-rich, polymict conglomerate (see Parras and Casadío, 2005). Greenish grains interpreted as glaucony (see below) are visually prominent (10%). Skeletal material (bivalves, barnacles, gastropods and echinoids) is disarticulated, fragmented, and bored, and lithic clasts consist of siliciclastic mudstone, coal, and thin, locally rounded, lenticular blocks (10 s of centimeters in length) of microcrystalline siderite. At Playa La Mina, the equivalent ravinement paleosurface is overlain by a thinly interbedded succession of siltstone, fine grained lithic arenite, allochemic arenites, and very thin (1–2 cm) discontinuous beds of microcrystalline siderite. Overlying this succession is a similar skeletal-rich polymictic conglomerate as at Cabo Curioso. Siderite, reworked or *in situ*, does not appear stratigraphically higher at either section. At Cabo Curioso, siderite clasts contain rare fragmented trapeziform and biolobate phytoliths or opaline cellular plant fossils (Madella et al., 2005); at Playa La Mina, glaucony is present with other cryptocrystalline grains.

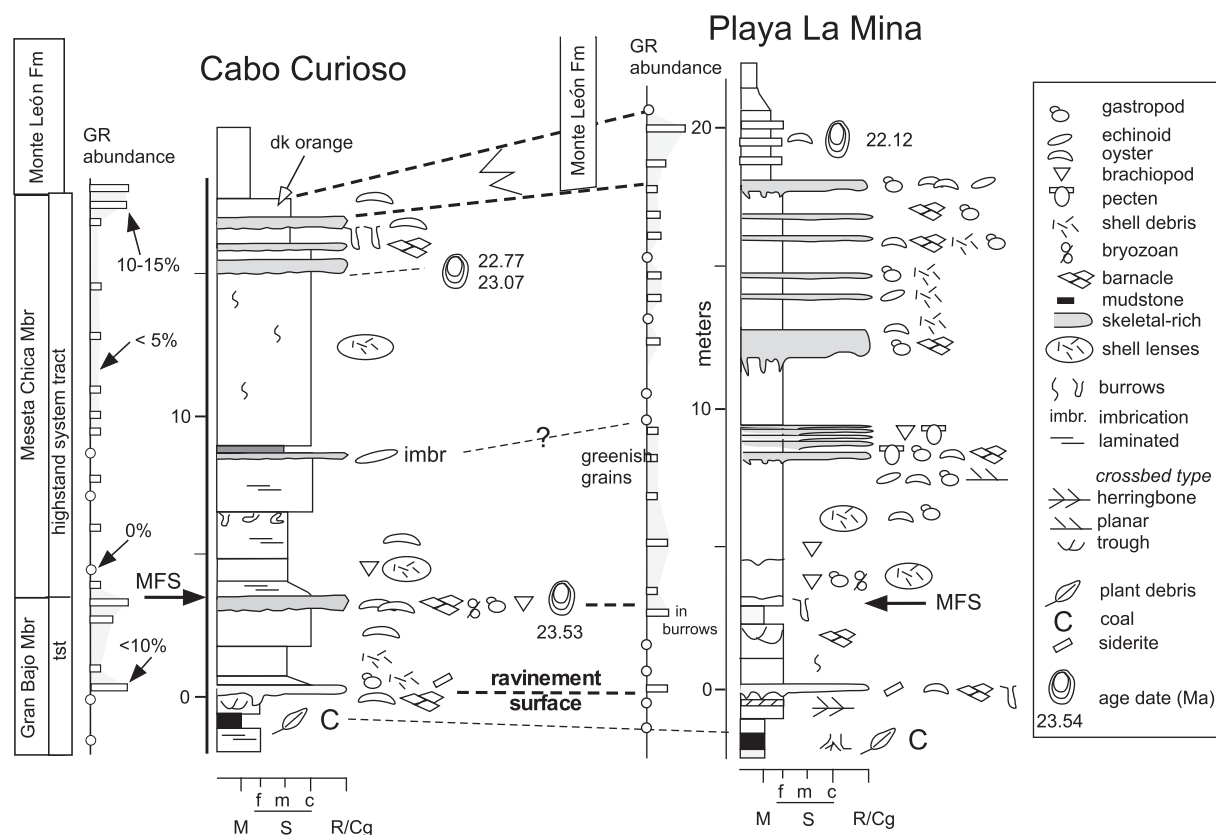


Fig. 4. Lithic successions at coastal sections, Cabo Curioso and Playa La Mina. Abbreviations: MFS, maximum flooding surface; GR abundance refers to stratigraphic abundance of greenish cryptocrystalline grains interpreted as autochthonous glaucony.

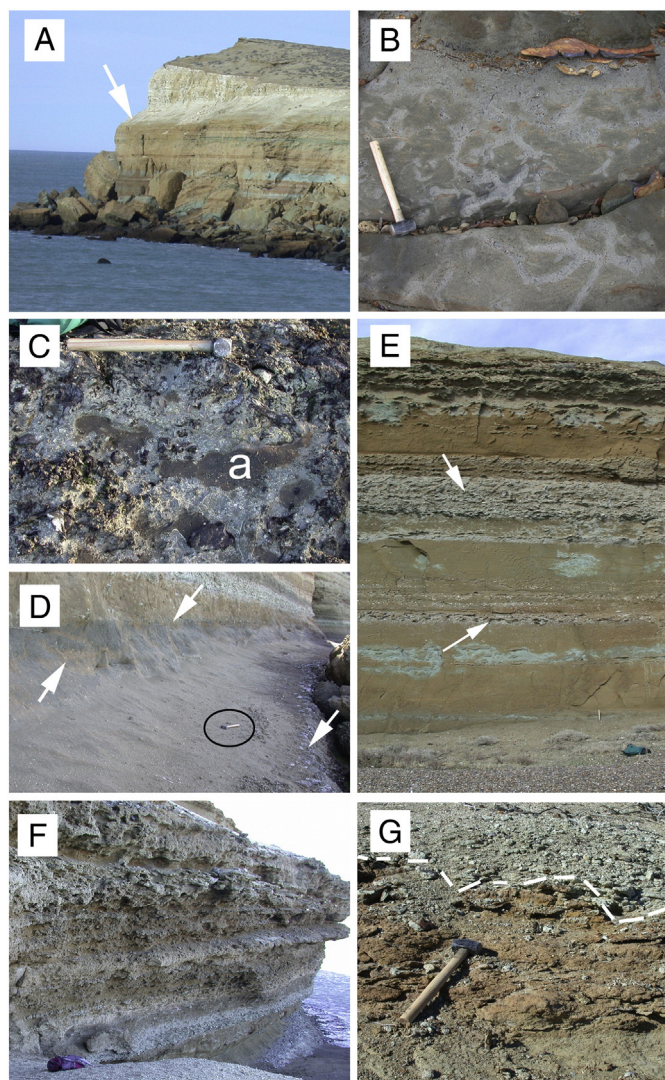


Fig. 5. Field photographs of selected stratigraphic features. A) Overview of the oxidized (orange) and reduced (green) succession (~15 m) of the Meseta Chica Member (upper San Julián Formation), and the contact (arrow) with the overlying tuffaceous (white) muddier Monte León Formation. Playa La Mina section. B) Lower ravinement surface consisting of locally heavily burrowed coastal plain sandstone and glauconitic burrow-fill arenite, and local siderite bed (orange). Playa La Mina section; hammer for scale. C) Lenses of glauconitic, and brachiopod- and mollusk-bearing, arenite within skeletal rudstone forming the upper level of the transgressive system tract at the Cabo Curioso section. The hammer (for scale) lies on the maximum flooding surface. D) Maximum flooding surface (lower arrow) at the Cabo Curioso section is overlain by clay-cemented lithic arenite (gray). The surface of this latter deposit is heavily burrowed (upper arrow) and overlain by sparsely allochemic oxidized arenite with intergranular calcite cement. E) Highstand succession exposed at the Playa La Mina section. Layers of skeletal rudstones (arrows) form resistant weathering surfaces whereas the arenitic intervals contain zones of reduction (green) that follow bedding, burrows, and areas of skeletal bearing sediment lenses. Vertical view is ~15 m. F) Highstand succession at the Cabo Curioso section showing a more densely stratified succession of skeletal rudstones. Vertical field of view ~8 m. G) Contact (dashed white line) between orange allochemic and glauconitic arenite and patchily distributed microcrystalline limestone and the overlying muddier lithic wacke. Cabo Curioso section. Hammer for scale.

4.2. Maximum flooding surface: Gran Bajo–Meseta Chica member boundary

At Cabo Curioso, the maximum flooding surface coincides with the top of a 20-cm thick sandy skeletal-rudstone dominated by shells, in life-position, of the giant oyster *Crassostrea? hatcheri* (Parras and Casadío, 2005). At Playa La Mina, an equivalent skeletal rudstone is absent. Instead, a unit of glauconitic (<10%) allochemic lithic arenite fills

large *Thalassinoid*-like burrows extending down into a 15-cm-thick silt-stone (Fig. 4).

At Cabo Curioso, oyster deposits represent skeletal–hiatal concentrations (Parras and Casadío, 2005). Oyster shells are differentially encrusted by bryozoans, serpulid worm tubes, and barnacles; and, they are heavily bored by polychaetes, bivalves, sponges, bryozoans and fungi (Parras and Casadío, 2005). The large size of the oysters created abundant (<40%) shelter paleoporosity, within which matrix sediment includes fragmented skeletal (brachiopod, molluscan, bryozoan) shells, crystalline and cryptocrystalline silicate grains, including glaucony, dispersed in local masses of micrite and abundant diagenetic void-fill calcite. Irregular shaped burrows and horizontal excavation cavities extend through the skeletal–hiatal deposit, but interconnected with the maximum flooding surface (Fig. 5C). An initial sediment fill is gray allochemic lithic arenite with <5% dark-green glaucony and mostly whole shells of bivalves and a terebratulid brachiopod, *Pachymagas*. This generation of sediment fill is cut by a second phase of burrowing and sediment fill, the latter a dark greenish gray glauconitic lithic arenite (Fig. 5C).

4.3. The highstand systems tract: Meseta Chica Member

At Cabo Curioso, ~1.5 m of non-calcareous to calcareous gray lithic arenite defines the lowermost highstand sediment overlying the bio-encrusted maximum flooding surface (Fig. 5D). The upper boundary of this unit is irregular with connected underlying burrows, and is overlain by orange-colored mixed sediment (Fig. 5D) typical of the remaining highstand section. At Playa La Mina, the lowermost highstand succession consists of reddish-orange lithic arenite to allochemic lithic arenite, in contrast to a mostly orange color in the rest of the section (Fig. 5A).

The predominant highstand lithologies at both Cabo Curioso and Playa La Mina are allochemic lithic to feldspathic arenite, less common non-calcareous siliciclastic beds, and prominent decimeter- to meter-scale coarsening-upward composite beds of more resistant, sandy, oyster-dominated (*C. hatcheri*; Parras and Casadío, 2005) skeletal rudstone to floatstone (Figs. 4, 5E, F). The latter facies is whitish gray in color, providing a prominent color contrast in outcrop (Fig. 5E, F). The rudstones overlie paleosurfaces that are often irregular to scalloped in geometry, and exhibit evidence of bioturbation. Thicker (40 cm–1.5 m thick) carbonate beds exhibit local stratification and crossbedding, indicative of high-energy transport (Parras and Casadío, 2005). The matrix of these deposits consists of glauconitic (<5%) skeletal grainstone or allochemic lithic to feldspathic arenite with local pockets of micrite, and abundant diagenetic calcite filling abundant (<40%) paleoporosity. Thinner (<30 cm) beds have more abundant sand- to mud-size sediment producing more skeletal floatstone, allochemic lithic arenite, and rare allochemic lithic wacke. In sandstones, oysters are less common, and skeletal material consists of fragmented to whole shells of pectens, gastropods, bryozoans, echinoids, decapods, and terebratulid brachiopods.

4.4. San Julián–Monte León formation boundary

The formation contact at Cabo Curioso is an irregular surface (Fig. 5G) that caps a coarse-grained, brownish orange, glauconitic (<15%) and calcareous allochemic arenite. This facies forms the uppermost (~40 cm) part of the formation at this locality. The arenite contains patchy domains of hard microcrystalline calcite, abundant Fe-oxide, and chalcedony; and, oyster shells are disarticulated, fragmented, and bored. Lower mixed-sediment beds have less Fe-oxide, no chalcedony, and much less skeletal fragmentation. Overlying the irregular formation boundary is greenish gray, weakly calcareous, glauconitic (<15%) silt-stone and lithic wacke of the lowermost Monte León Formation (Fig. 5G). At Playa La Mina, a similar glauconitic lithofacies forms the lowermost Monte León Formation, along with reworked and *in situ*

oyster shells of *C. hatcheri* (Fig. 4; Parras et al., 2012). Uppermost strata of the San Julián Formation consist of a medium-grained allochemic arenite showing none of the accessory attributes of equivalent strata at Cabo Curioso.

4.5. Siliciclastic grain types and their stratigraphy

Siliciclastic grains are divisible into two groups. The first consists of reworked angular to subrounded crystalline grains that include feldspar porphyry and other volcanic-derived lithoclasts (30–60%), plagioclase (<15%: albite and andesine), dusty (clay-altered) potassium feldspar (10%), and minor quartz (5%). There is no obvious stratigraphic variation in abundance of minerals or rock fragments in either section. The detrital clay fraction throughout the sections consists of a mixture of kaolinite, illite, and chlorite.

The second group consists of rounded cryptocrystalline grains with end-member colors of green, brown, red, and yellow (Fig. 6). Related microfabrics and morphologies include: rare detrital crystalline silicate or lithic (volcanic) cores (Fig. 6A–B); microfractures that widen toward

the grain margin, and are sites of discoloration or contain fill by additional cryptocrystalline silicate of another color (Fig. 6C–E); and, irregular brownish to yellow-brown grain margins that grade into greenish cores (Fig. 6D). Light to dark green and brownish green grains display an irregular rounded micromorphology (Fig. 6D), whereas other colored grains are very well rounded (Fig. 6), and usually ovoid in cross-section (Fig. 6A–B). At Cabo Curioso, reddish brown grains are locally replaced by chalcedony (Fig. 6F) in the uppermost (40 cm) part of the formation.

Greenish grains form the only fraction to display changes in stratigraphic abundance (Fig. 4). Increased abundances (up to 20%) occur in sediment within ~1 m above the ravinement surface in the Gran Bajo Member; within the skeletal–hiatal deposit beneath the maximum flooding surface at Cabo Curioso, and equivalent burrow-fill allochemic arenite at Playa La Mina; within skeletal concentrations in the highstand succession; and, within strata bounding the San Julián–Monte León formation boundary. In the San Julián Formation, dark greenish grains are dominant whereas there is a 30:70 admixture of light to dark green grains in the uppermost (40 cm) unit at Cabo Curioso, but only light green grains occur in the overlying lower Monte León Formation.

Compositional differences among grain colors (Supplemental Table S2) are revealed by major oxide concentrations (Fig. 7). Greenish and yellow grains fall on a common trend, with yellow grains (found only at Cabo Curioso) containing greater Al_2O_3 content, and red and orange grains (Fig. 6A) are enriched in Fe_2O_3 (Fig. 7). Dark green grains display increased Fe^{3+} and K^+ concentrations (Fig. 8), and discoloration (green to brown) along rims and microfractures is associated with increased concentrations of Al^{3+} and Fe^{3+} at the expense of K^+ (Fig. 8).

5. Diagenetic attributes

5.1. Non-carbonate components

5.1.1. Clay cement

Authigenic illite forms intergranular isopachous cement (Fig. 9A) in non-calcareous arenites at three stratigraphic positions: (1) in fine-grained arenite beneath the ravinement surface at both sections; (2) in lithic arenite that overlies the maximum flooding surface at Cabo Curioso; and, (3) in less common non-calcareous lithic arenites higher in the highstand succession at both sections. Clay cement post-dates formation of intergrain point contacts and shows increased crystal size and intercrystalline porosity toward centers of intergranular pore space (Fig. 9A).

5.1.2. Zeolite cement

Zeolite forms common (5–10%) intergranular cement in beds of allochemic lithic arenite and polymict conglomerate within 1 m above the ravinement surface in both sections. Crystals are <100 μm in length, clear to slightly purplish in transmitted light, and have columnar to thin plate shapes in cross-section (Fig. 9B). Crystal growth occurred after the formation of point and long intergrain contacts, and predate calcite cement that occludes the remaining porosity. Rare and much smaller columnar zeolite crystals (5–20 μm) post-date or overlap formation of cryptocrystalline Fe-oxide that coats margins of present-day porosity in the highstand succession (Fig. 9D).

Columnar and platy crystal shapes have a common geochemistry based on electronic microprobe analysis (Supplemental Table S1): ~71 wt.% SiO_2 ; ~4.3 wt.% K_2O ; and, a Si/Al atomic ratio of ~4.3. This identifies a possible silica-rich clinoptilolite-K (e.g., Wise et al., 1969; Oscarson and Bargar, 1996; Ogihara, 2000; Morbidelli et al., 2001). The Al_2O_3 content (~14%) is higher than expected (~12 wt.%), and may identify extra aluminum as an extra framework cation (Armbruster, 2001).

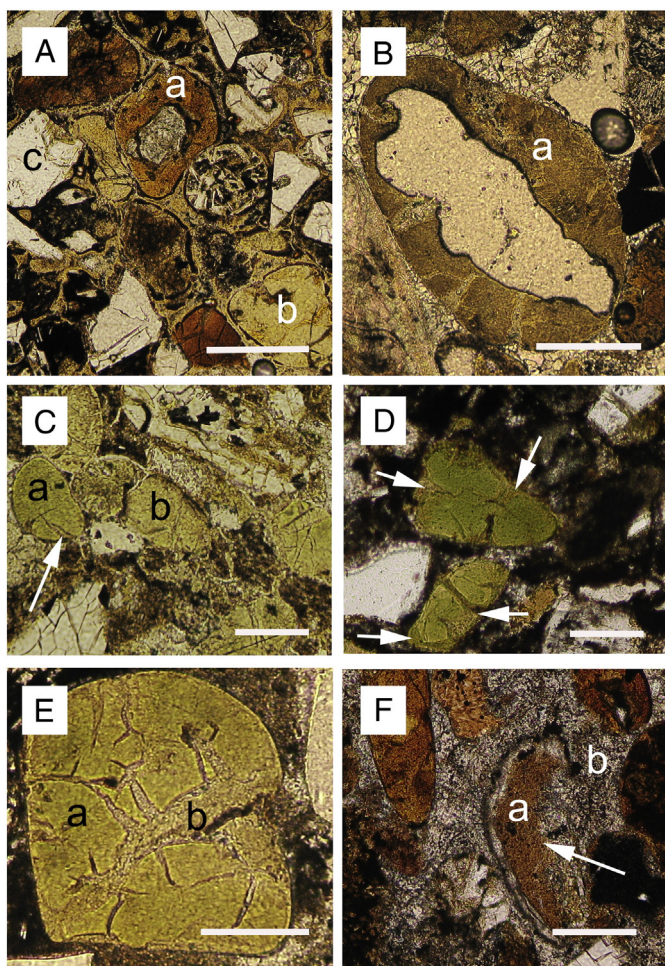


Fig. 6. Colored cryptocrystalline grains; all polarized light photomicrographs. A) Three types of cryptocrystalline silicate habits: rim (a) with a core of a volcanic lithic fragment; uniformly cryptocrystalline yellowish grain (b); and silicate grain (c) locally altered by cryptocrystalline silicate along microfractures. Scale bar is 250 μm . B) Brownish cryptocrystalline rim (a) around solution-etched crystalline silicate grain; scale bar = 100 μm . C) Light green grains (a) with microfracture containing yellowish green clay similar to the composition of an adjacent grain (b); scale bar = 200 μm . D) Dark green grains with circumgranular brownish alteration extending into the core along microfractures (arrows); scale bar = 100 μm . E) Yellow-green grain (a) showing multiple microfractures along which there is yellowish cryptocrystalline fill or alteration. Scale bar = 50 μm . F) Orange cryptocrystalline grains differentially replaced by silica that also replaces adjacent matrix. Scale bar = 100 μm .

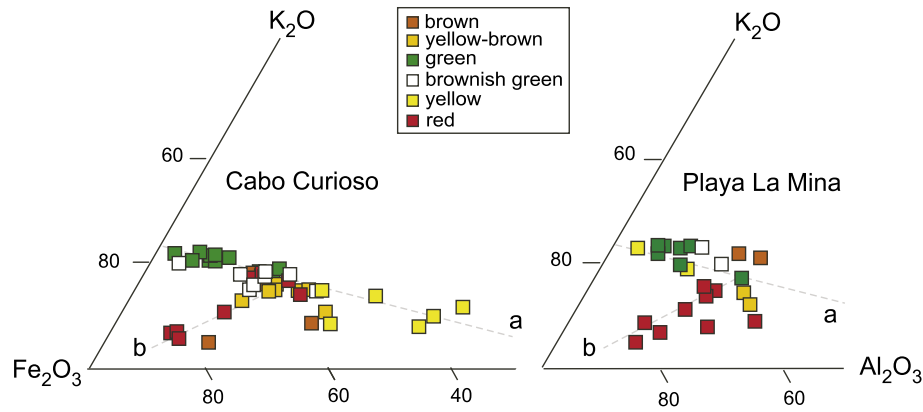


Fig. 7. Ternary plot of major oxide (K, Al, Fe) concentrations in cryptocrystalline grains.

5.1.3. Chalcedony and Fe-oxide

Chalcedony appears only in the orange allochemic arenite at the top of the San Julián Formation at Cabo Curioso. It occurs as a local replacement of oyster shell calcite and brownish red cryptocrystalline grains

(Fig. 6F), and fills subhorizontal (to bedding) microfractures that cross-cut domains of diagenetic microcrystalline calcite.

Excluding the lowermost ~1.5 m of the highstand succession at Cabo Curioso, Fe-oxide is otherwise pervasive in mixed sediment, providing the prominent orange coloration (Fig. 5A, E). At both sections, patchy and bed-parallel distributions of green-colored rock surfaces (Fig. 5E) represent zones of iron reduction. In thin section, Fe-oxide forms an intergranular discontinuous coating on silicate and carbonate grains, replaces local clay cement and matrix in arenites, and line surfaces of extant moldic and intergranular porosity. In the uppermost allochemic arenite of the San Julián Formation at Cabo Curioso, Fe-oxide as patches of densely distributed euhedral micron-scale crystals replace arenite

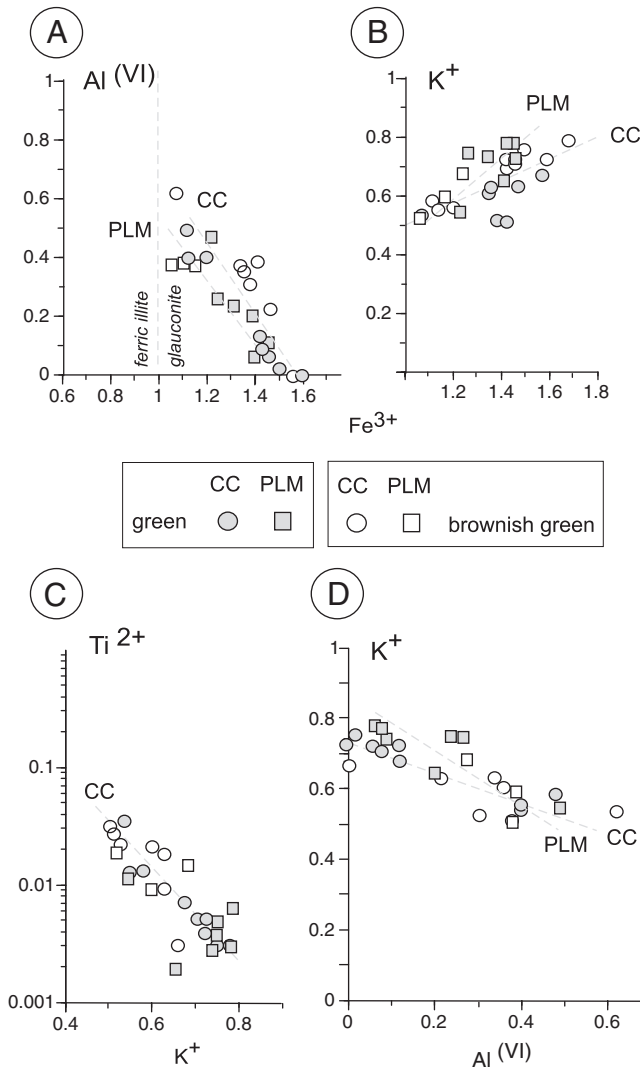


Fig. 8. Lattice composition of Fe^{3+} , $\text{Al}^{(\text{IV})}$, $\text{Al}^{(\text{VI})}$, Ti^{2+} and K^{+} in green and brownish green cryptocrystalline grains that are interpreted to be autochthonous glaucony. The boundary for ferric illite is from Longuépée and Cousineau (2006).

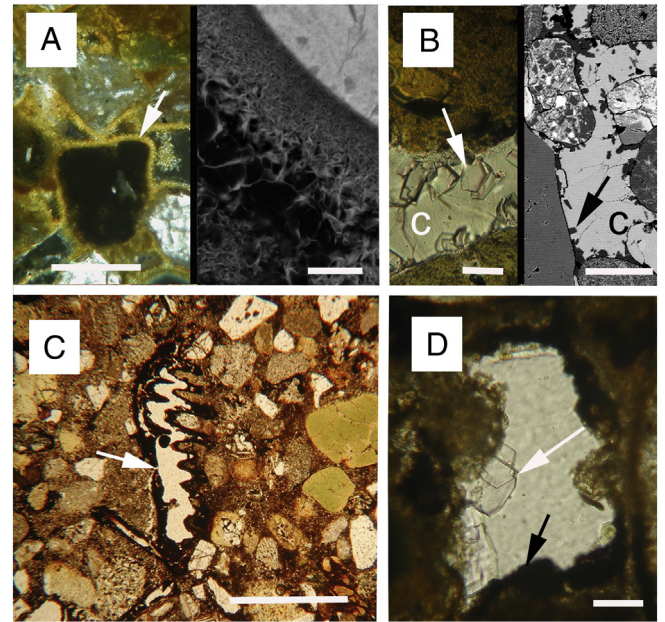


Fig. 9. A) Intergranular clay cement: (left) Isopachous clay cement (arrow) within lithic arenite above the maximum flooding surface, Cabo Curioso. Thin section photomicrograph, polarized light; scale bar is 250 μm ; (right) intercrystalline porosity and crystal size of clay cement increase toward the intergranular pore center. Backscatter scanning electron photomicrograph; scale bar is 10 μm . B) Zeolite crystals: (left) platy crystal (arrow) forming initial intergranular cement, followed by calcite (c) cement. Transmitted plain light; scale bar is 20 μm . (right) Columnar crystals (black) forming initial cement followed by calcite (c) cement. Backscattered electron photomicrograph; scale bar is 200 μm . C) Fe-oxide-replaced oyster shell (arrow) with partially developed moldic porosity (white area). Uppermost (< 40 cm) San Julián Formation, Cabo Curioso section; scale bar is 250 μm . D) Remnant microporosity with discontinuous rim of iron oxide (black arrow), and local microcrystals of zeolite (white arrow). Scale bar is 20 μm . (For interpretation of the references to color in this figure legend, the reader is referred to the web version of this article.)

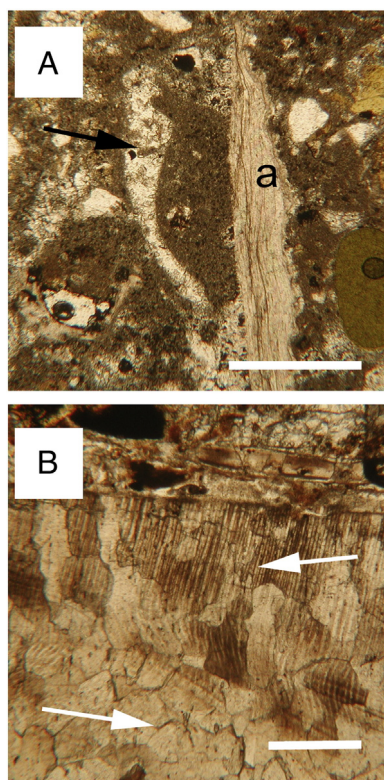


Fig. 10. A) Fibrous oyster shell (a) in micrite/microsparite (brown) adjacent to paleoporosity now filled with calcite cement (arrow) that has a curved geometry similar to aragonitic bivalve shells. Scale bar is 500 μm . B) Brown crystalline mosaic of replacement calcite demonstrated by relict fibrous fabric (upper arrow) likely associated with an aragonitic bivalve shell. The replacement calcite appears continuous into the adjacent paleovoid space (lower arrow). Transmitted plain light; scale bar is 300 μm . (For interpretation of the references to color in this figure legend, the reader is referred to the web version of this article.)

matrix and oyster shell calcite, and fills microfractures through chalcidony and diagenetic microcrystalline calcite. Complete replacement of oyster-shell calcite results in local formation of secondary (moldic) porosity (Fig. 9C).

5.2. Carbonate components

5.2.1. Skeletal microfabric

Fibrous punctate terebratulid calcite is well preserved but punctae are filled with framboidal pyrite and orange luminescent microcrystalline

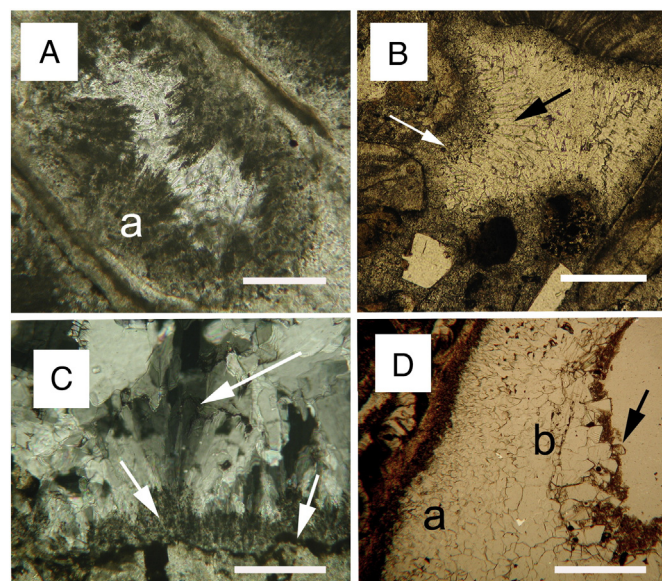


Fig. 11. A) Intraskeletal microfibrillar calcite cement (a) forming an irregular but isopachous deposit within a bryozoan skeleton. Inclusion-poor microcrystalline calcite fills the remaining pore space. Thin section, transmitted plain light; scale bar is 125 μm . B) Inclusion-rich isopachous fibrous to microcrystalline calcite cement (white arrow) with remaining space filled by inclusion-free bladed calcite cement (black arrow). Thin section photomicrograph, transmitted plain light; scale bar is 100 μm . C) Locally etched and iron-oxidized surface of oyster shell (lower arrow) overlain by inclusion-rich fibrous calcite cement (middle arrow), then splay of inclusion-poor bladed calcite cement (upper arrow). Thin section photomicrograph, cross-polarized light. Scale bar is 250 μm . D) Equant calcite cement displaying increase in crystal size (a to b) toward center of the paleocavity. Cement is overlain by a cryptocrystalline layer of Fe-oxide and rare zeolite microcrystal (arrow). Thin section photomicrograph, transmitted plain light. Scale bar is 200 μm . (For interpretation of the references to color in this figure legend, the reader is referred to the web version of this article.)

calcite (see Parras et al., 2012). Fibrous oyster calcite often appears well preserved (Fig. 10A), but some shells exhibit zones of fiber-parallel luminescence identifying intraskeletal alteration (Parras et al., 2012). The expected fibrous fabric of aragonitic bivalve shells (Bathurst, 1975) is rarely present. Paleomolds with curvatures similar to bivalve fragments are preserved in microcrystalline calcite matrix (Fig. 10A), and filled with luminescent equant calcite cement. In allochemic arenites, similar shaped shell fragments consist of a brownish (in plain light) microcrystalline mosaic of calcite within which is a poorly preserved relict fibrous fabric (Fig. 10B). The calcite luminesces orange and appears continuous with intergranular void-fill calcite cement (Fig. 10B). Gastropods are also originally of aragonite, but in these sections consist of microcrystalline

Table 2
Primary and diagenetic pore-filling calcites.

Type	Distribution	Characteristics	Interpretation
1. Micrite	Shelter porosity; - below/on maximum flooding surface; in highstand skeletal rudstones	Dark to light brown (plain light); relict within masses of microsparite; heterogeneous texture; dull CL, with brighter patches in less homogeneous masses	Marine, magnesian calcite; depositional
2. Microsparite	Shelter porosity; - below maximum flooding surface; highstand skeletal rudstones	Forms masses with or without relict micrite; heterogeneous crystal size; moderate to bright CL	Neomorphosed micrite; low-Mg calcite
<i>Cements</i>			
3. Fibrous calcite	Intraskeletal porosity; - bryozoans, barnacles	Turbid (micritic) to clear crystals; forms isopachous layers; grades laterally into microsparite layers; patchy dull orange CL	Marine, magnesian calcite cement
4. Syntaxial	Intergranular porosity	Fine- to coarsely crystalline; incorporates echinoderm plates prior to complete mechanical compaction; dull CL	Phreatic, low-Mg calcite cement
5. Bladed	Shelter porosity, other intergranular porosity	Crystal splays, isolated or forming isopachous layers; post-dates mechanical compaction; dull to moderate orange CL	Burial phreatic, low-Mg calcite cement
6. Equigranular	Intergranular porosity	Euhedral crystalline mosaics; in larger pore space with increasing crystal size, and consecutive dull to bright CL, toward center of pore space; last stage of pore-filling carbonate	Burial phreatic, low-Mg calcite cement

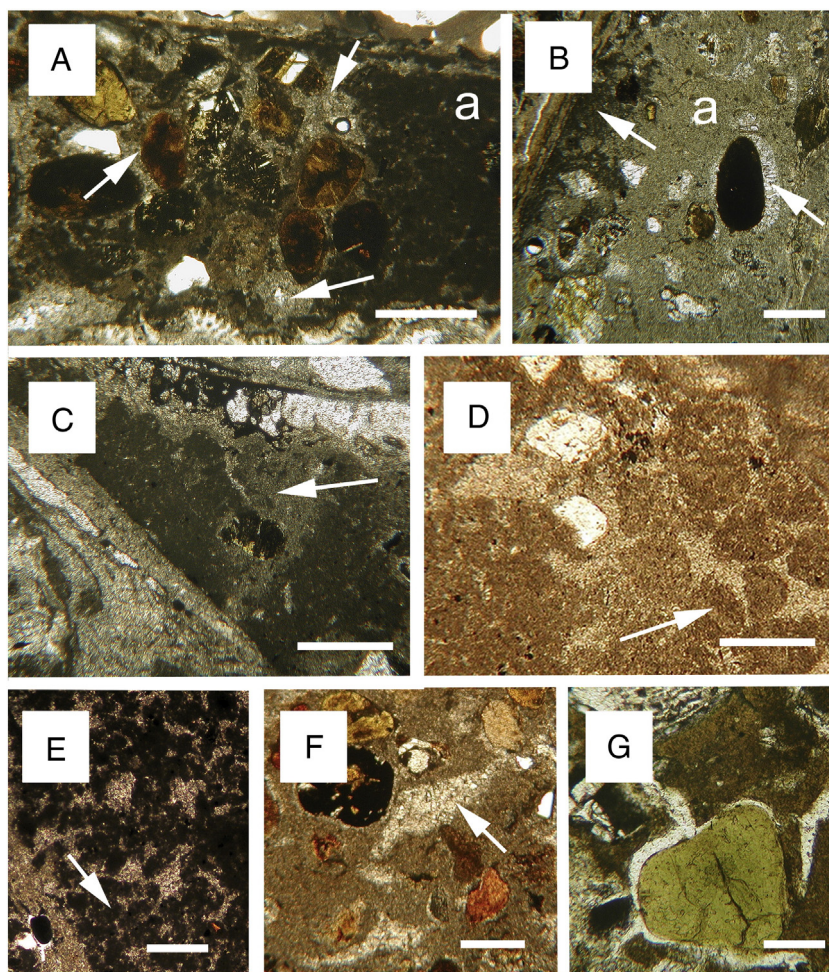


Fig. 12. Photomicrographs (transmitted plain light) of micrite, microsparite, and related textures. A) Micrite (a), with microburrows or tubules filled with microsparite (arrows), contains small areas of microsparite (arrows), preferentially positioned adjacent to cryptocrystalline grains (reddish brown). Scale bar is 250 μm . B) More fully developed microsparite (a) with filigree micritic fabric extending from shell fragment (left arrow). A circumgranular paleocavity filled with microsparite is developed marginal to a silicate grain (right arrow). Scale bar is 100 μm . C) Area of microsparite (arrow) extends around a silicate grain, and displays gradational boundaries with micrite (dark). Scale bar is 125 μm . D) Peloid-like texture (arrows) of microsparite. Scale bar is 50 μm . E) Filigree micritic fabric within microsparite. Scale bar 100 μm . F) Sinuous paleocracks (arrow) filled with microcrystalline calcite cement within microsparite. Scale bar is 150 μm . G) Artificially produced circumgranular and sinuous cracks in clay-rich matrix. Scale bar is 100 μm . (For interpretation of the references to color in this figure legend, the reader is referred to the web version of this article.)

calcite. In the upper 4 m of the section at Playa La Mina, gastropod steinkerns (or shell molds) are preserved in very hard microcrystalline calcite.

5.2.2. Calcite cement

Several calcite cement types (Table 2) are associated with the marine portion of the transgressive-highstand succession. In the skeletal-hiatal deposit beneath the maximum flooding surface, isopachous microfibrous calcite with a dull orange luminescence forms a common cement within intraskeletal and intergranular porosity (Fig. 11A–B). This cement type is associated with the 1st-generation burrow fill beneath the maximum flooding surface whereas the 2nd generation burrow-fill contains equant intergranular calcite as described above. Within paleopore space, inclusion-rich microsparite with or without relict fibrous fabric appears to grade laterally into well preserved microfibrous calcite. The microsparite has a brighter orange luminescence. Very locally, the microfibrous and equivalent microcrystalline cement overlie etched Fe-oxidized surfaces of calcitic shell material (Fig. 11C).

The two most abundant cement types in oyster-dominated skeletal rudstone are crystal splays (<500 μm in width) of bladed calcite, and masses of equant crystalline calcite (Table 2). The first almost always overlies a layer of microfibrous or inclusion-rich microcrystalline calcite

cement (Fig. 11B–C), and has an orange-red luminescence. There is no preferred orientation of splays, and some juxtaposed splays produce an isopachous layer in larger paleoporosity. The second cement type forms equant crystal mosaics that completely and partially fill remaining shelter porosity, and, in the highstand succession, is overlain by cryptocrystalline Fe-oxide and rare zeolite crystals (Fig. 11D). In larger paleocavities, crystal size increases toward the center of the paleopore space (Fig. 11D). A third, but local, cement, consists of syntaxial overgrowth cement of low-Mg calcite developed around echinoderm fragments that predates completion of mechanical compaction.

Two cement types associated with allochemic arenites include local development of syntaxial overgrowth cement (as above), and a predominant equant calcite that luminesces orange and post-dates development of intergranular (long, point) grain contacts. This cement is similar petrographically to the final cement in skeletal rudstone. Above the ravinement surface, this cement follows zeolite cement (Fig. 9B), and replaces quartz and feldspar grains.

5.2.3. Masses of microcrystalline calcite

Microcrystalline calcite is represented by micrite (<4 μm) and microsparite (4–30 μm) that form local intergranular masses occupying shelter porosity in oyster-dominated skeletal rudstone (Fig. 12). Siliciclastic grains and skeletal fragments are dispersed (or float) within

Table 3
Elemental geochemistry (weight percent) of calcite^a.

Playa La Mina																
	Bivalve (altered) n = 9		Micrite n = 7		Microspar n = 3		Fibrous cement n = 10		Bladed cement n = 7		Equant calcite n = 34		Silicate (replaced) n = 3			
	x	σ	x	σ	x	σ	x	σ	x	σ	x	σ	x	σ		
Ca	37.98	0.94	38.01	1.74	39.11	0.64	38.68	0.70	38.78	1.07	37.39	1.40	38.93	1.65		
Fe	1.05	0.30	1.14	0.46	0.96	0.16	0.78	0.28	0.84	0.27	1.08	0.55	0.99	0.18		
Mn	0.75	0.77	0.80	0.57	0.52	0.09	0.39	0.21	0.93	0.51	1.31	1.04	1.20	0.76		
Mg	0.36	0.09	0.43	0.20	0.41	0.06	0.25	0.09	0.35	0.21	0.48	0.24	0.52	0.07		
Sr	0.01	0.01	0.00	0.00	0.00	0.00	0.01	0.02	0.00	0.01	0.05	0.13	0.01	0.01		
Na	0.03	0.02	0.05	0.03	0.03	0.02	0.02	0.01	0.03	0.03	0.07	0.14	0.03	0.03		
Sr (max)	0.01		0.00		0.00		.05		.03		0.47		0.02			
Na (max)	0.09		0.09		0.04		.04		.07		0.45		0.05			
Skeletal calcite																
	Bivalve n = 6				Echinoid n = 3						Oyster n = 4					
	x	σ			x	σ					x	σ				
Ca	38.61			0.73	39.12			0.16			39.04			0.38		
Fe	0.20			0.29	0.05			0.05			0.05			0.03		
Mn	0.09			0.18	0.01			0.01			0.03			0.02		
Mg	0.31			0.08	0.94			0.03			0.30			0.04		
Sr	0.38			0.04	0.15			0.00			0.37			0.05		
Na	0.50			0.11	0.17			0.01			0.49			0.20		
Cabo Curioso																
	Micrite		Microspar		Fibrous cement		Bladed cement		Equant cement		Microspar in cracks		Silicate (replaced) overgrowth		Syntaxial	
	n = 3		n = 14		n = 8		n = 28		n = 30		n = 11		n = 3		n = 6	
	x	σ	x	σ	x	σ	x	σ	x	σ	x	σ	x	σ	x	σ
Ca	37.73	2.22	37.89	1.50	37.45	1.84	38.86	1.00	38.90	1.75	38.94	0.54	39.95	0.15	38.60	0.51
Fe	1.26	0.92	1.14	0.84	1.07	0.49	0.71	0.27	0.94	0.45	0.48	0.20	0.42	0.09	0.86	0.12
Mn	0.43	0.47	1.04	1.05	1.93	0.90	0.54	0.44	0.90	0.93	0.25	0.30	0.71	0.61	0.42	0.25
Mg	0.40	0.12	0.43	0.21	0.49	0.30	0.53	0.25	0.46	0.24	0.26	0.12	0.14	0.03	0.40	0.06
Sr	0.00	0.00	0.00	0.00	0.01	0.01	0.01	0.01	0.00	0.01	0.00	0.01	0.00	0.00	0.00	0.00
Na	0.28	0.29	0.03	0.03	0.03	0.02	0.01	0.01	0.01	0.01	0.01	0.01	0.02	0.01	0.01	0.01
Sr (max)	0.01		0.01		0.02		0.03		0.02		0.02		0.00		0.00	
Na (max)	0.61		0.01		0.05		0.04		0.05		0.03		0.02		0.03	
Skeletal calcite																
	Bivalve n = 7				Oyster n = 11				Barnacle n = 4				Bryozoan n = 3			
	x	σ			x	σ			x	σ			x	σ		
Ca	39.03			0.42	38.02			1.60	38.83			0.36	37.81			0.21
Fe	0.29			0.18	0.30			0.40	0.11			0.06	0.96			0.58
Mn	0.30			0.48	0.21			0.31	0.02			0.02	0.80			0.11
Mg	0.27			0.14	0.40			0.30	0.24			0.08	0.64			0.54
Sr	0.12			0.16	0.29			0.12	0.39			0.05	0.00			0.00
Na	0.22			0.13	0.31			0.12	0.43			0.07	0.01			0.02

^a x, mean; σ, standard error; mx, maximum value.

the void-fill carbonates. Micrite displays an inhomogeneous texture related to locally admixed clay particles, local patches of microsparite, and elongate, decimicron-scale microburrows or tubules of microspar (Fig. 12A–C). A gradational boundary of changing crystal size divides adjacent masses of micrite and microsparite. Areas of microsparite in micrite are often positioned around silicate grains that were originally interred within the micrite (Fig. 12C). Peloidal or pseudopeloidal textures (Tucker and Wright, 1990) are locally developed in microsparite (Fig. 12D), as is a delicate micritic filigree fabric (Fig. 12E). Sinuous to crescent-shaped paleocavities (Fig. 12F), including circumgranular paleocracks (Fig. 12B), are filled with luminescent equant calcite cement. The paleocavities are similar to artificial shrinkage cracks in local clay-rich matrix (Fig. 12G).

5.2.4. Trace element geochemistry

Skeletal carbonate, micrite, microsparite, and carbonate cements are low-Mg (<0.5 wt.%) calcite and, generally, Fe-poor (~1 wt.%; Table 3). Mn concentrations vary between and within a given calcite type (Table 3), with the highest values (2–3 wt.%) associated with equant calcite cement in allochemic arenites and shelter porosity in skeletal rudstones. The majority of skeletal and void-fill calcites have low (<250 ppm) or undetected (<100 ppm) Sr and Na concentrations (Fig. 13A–B). Well preserved (as defined petrographically) oyster-shell calcite at Cabo Curioso defines a steep (4:1) Na:Sr slope (Fig. 13A) similar to well preserved oyster calcites used in generating the Sr-isotope framework for the San Julián Formation (Fig. 13C; Parras et al., 2012). The data trend is common with other known Oligocene–Miocene

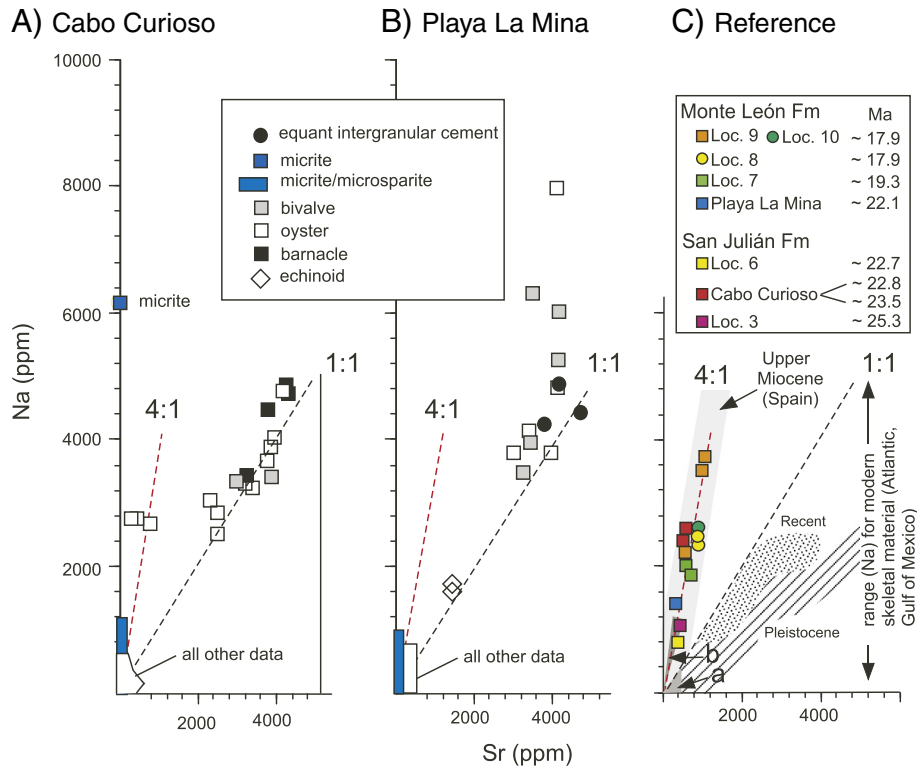


Fig. 13. Na:Sr ratio trends (4:1, 1:1) shown relative to concentrations in skeletal and void-fill calcites from A) Cabo Curioso, B) Playa La Mina, and C) Reference datasets. The latter include oyster-shell calcites used for the Sr-isotope framework of the San Julián and Monte León formations (Parras et al., 2012), and numbered localities refer to those in Fig. 1B and Table 1; Quaternary sediment, rock, and marine skeletal material (dotted and lined areas) from the Bahamas and Caribbean (Land and Hoops, 1973); Upper Miocene oyster shell calcite, Spain (grayed area: Lu, 2008); and Upper Oligocene oyster shell calcite, New Zealand (a) and the Puerto Madryn region (b), Argentina (MacMillan, 2010).

oyster-shell datasets (Fig. 13C) from Spain (Lu, 2008) and Argentina (MacMillan, 2010). At Cabo Curioso, all but one of the diagenetic carbonates (a micrite with ~6000 ppm Na) fall along a shallower (1:1) slope (Fig. 13A). Many diagenetic carbonates at Playa La Mina have Na values ranging above this ratio (Fig. 13B).

5.2.5. Isotope geochemistry

$\delta^{18}\text{O}$ and $\delta^{13}\text{C}$ paired values for siderite clasts at Cabo Curioso and beds at Playa La Mina are, respectively: -3.4% and $+10.8\%$, and -3.6% and $+5.9\%$. Isotope values for carbonate types (Supplemental Table S4) establish three general clusters (Fig. 14A) relative to a marine calcite field (a in Fig. 14A) defined by Oligocene–lower Miocene platform limestone in southern Australia (Kyser et al., 1998; Pufahl et al., 2006) and skeletal (oyster, pectinid) calcite in the San Julián Formation (Parras et al., 2012). Samples of brachiopod skeletal calcite from the two sections define a fairly steep negative trend away from this marine field (Fig. 14A). Diagenetic components from beneath the maximum flooding surface at Cabo Curioso form a relatively tight cluster (b in Fig. 14A) with a mean value of $\delta^{18}\text{O} \sim -12\%$ and $\delta^{13}\text{C} \sim -1\%$. A more dispersed array (c in Fig. 14A) associated with samples from the highstand succession at both sections displays $\delta^{18}\text{O}$ values intermediate to the two above fields whereas the $\delta^{13}\text{C}$ values are more negative, extending to -12% (Fig. 13A). Viewed stratigraphically, clusters b and c are associated with the marine transgressive and highstand succession, respectively (Fig. 14B). In the highstand succession, $\delta^{18}\text{O}$ and $\delta^{13}\text{C}$ values are very similar, and, at Playa La Mina, describe an upsection increase offset by a negative shift immediately beneath the Monte León Formation.

6. Discussion

Marine and burial diagenetic attributes of the San Julián Formation are stratigraphically constrained: that is, they are spatially associated with specific stratigraphic or depositional attributes of the host depositional system tract (Fig. 15). We discuss the origins of marine- and burial-derived diagenetic stratigraphies and their significance in a sequence stratigraphic context.

6.1. Glaucony stratigraphy and seafloor weathering

Cryptocrystalline greenish grains (i.e., light and dark green, and brownish green) are interpreted to be autochthonous glaucony according to their: (1) irregular rounded granular micromorphology (Amorosi, 1997); (2) geochemistry (Supplemental Table S2), when compared to glaucony in a variety of depositional environments (Takahashi, 1939; Hendricks and Ross, 1941; Burst, 1958; Buckley et al., 1984; Longuépée and Cousineau, 2006; Eder et al., 2007; Sánchez-Navas et al., 2008); (3) petrographic attributes, including microfractures (Sánchez-Navas et al., 2008); and, (4) crystal lattice inter-element correlations (Fig. 8, Supplemental Table S3; Ireland et al., 1983; Longuépée and Cousineau, 2006). Autochthonous glaucony in a shallow-water platform interior as defined by the San Julián Formation (Parras and Casadio, 2005) is part of its known depositional spectrum from shallow to deep-water settings (e.g., Porrenga, 1967; Amorosi, 1997; Chafetz and Reid, 2000; Hesselbo and Huggett, 2001).

The non-greenish cryptocrystalline grains are interpreted to represent reworked (allochthonous) altered glaucony (Amorosi, 1997). An apparent sustained stratigraphic abundance within the

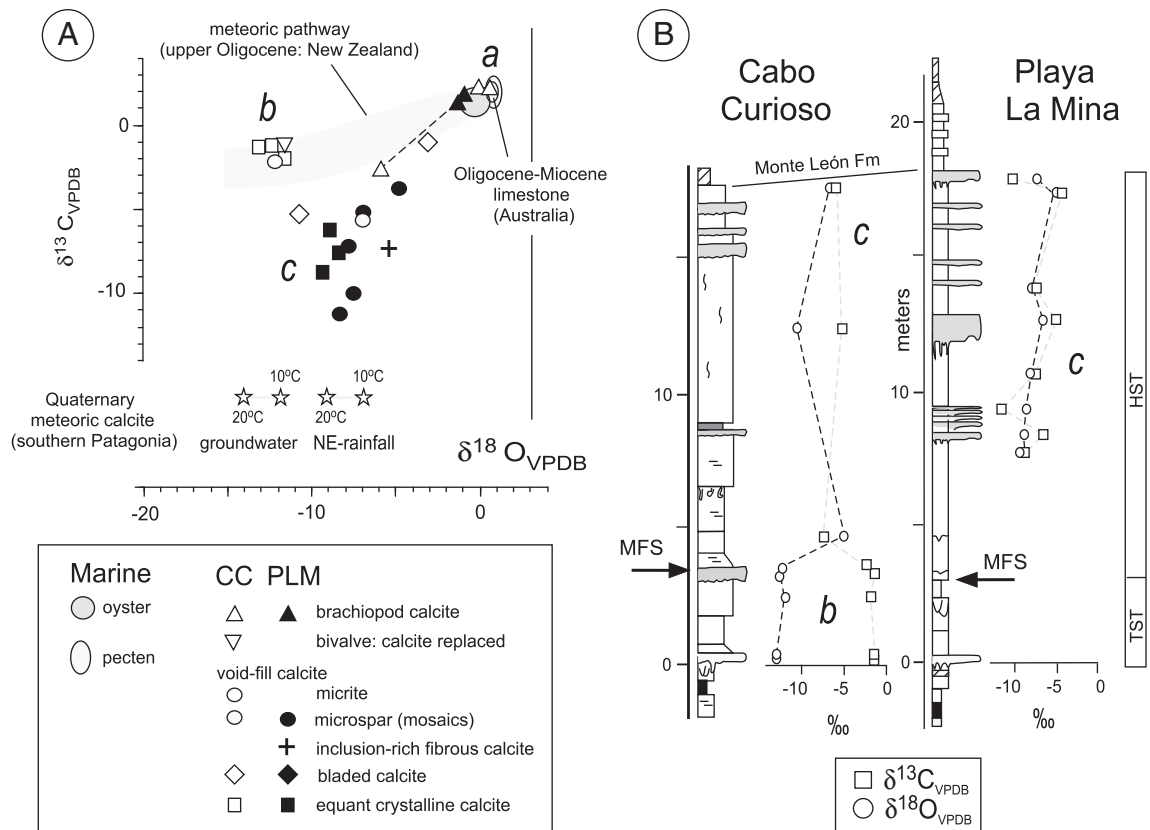


Fig. 14. (A) $\delta^{18}\text{O}$ and $\delta^{13}\text{C}$ values for skeletal and diagenetic carbonates at Cabo Curioso (CC) and Playa La Mina (PLM). Three clusters (a–c) are described in the text, and the dashed line represents a linear trend in brachiopod calcite (see text). Marine fields are based on: pecten and oyster calcite in the San Julián Formation (Parras et al., 2012); Oligocene–Miocene marine calcite, South Australia (Pufahl et al., 2006); meteoric calcite pathway, New Zealand (Dix and Nelson, 2006). Also shown are calculated isotope values for meteoric calcites if precipitated from present-day regional groundwater and NE-derived rainfall in central Patagonia (Mayr et al., 2012). (B) Stratigraphic distribution of oxygen and isotope values from diagenetic calcites in the San Julián Formation. Patterns are segregated by depositional system tracts (TST, transgressive system tract; HST, highstand system tract) bracketing the maximum flooding surface (MFS).

transgressive and highstand system tracts suggests that there was a relatively constant supply of altered grains transported from a more landward (coastal) source.

Dark-green autochthonous glaucony identifies a chemically-evolved state arising from extended exposure at the sediment–water interface (Odin and Matter, 1981; Amorosi, 1997). Within the marine transgressive–highstand succession of the San Julián Formation, this glaucony type is associated with stratigraphic intervals that define periods of extended seafloor reworking and/or seafloor exposure (Fig. 15). This includes: the basal (1 m) marine transgressive succession above the ravinement succession (Parras and Casadío, 2005); within skeletal–hiatal rudstone along and beneath the maximum flooding surface; and, within the skeletal (event-bed) deposits in the highstand succession. Extended seafloor exposure may also explain the distribution of unaltered oyster-shell calcites along the steep Na:Sr (4:1) slope (Fig. 13C). Clearly differentiated from diagenetic carbonate in our sections (Fig. 13A–B), trace element concentrations in oyster-shell calcite will vary according to oyster species, environmental and metabolic controls, and post-depositional diagenesis (Carriker et al., 1996). The first and last controls may be excluded with regard to our sections. Instead, local environmental controls influencing either uptake and/or loss of Na and Sr may be related to prolonged exposure on the seafloor (Carriker et al., 1991).

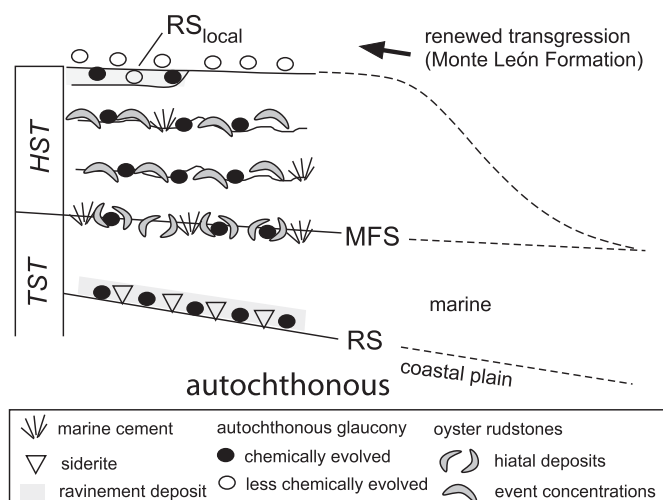
In comparison to chemically evolved glaucony, light-green (less chemically evolved) glaucony associated with the lowermost muddy Monte León Formation (Fig. 15) may identify a more rapid rate of burial (Amorosi, 1997). Admixture of these glauconies in the uppermost unit of the San Julián Formation at Cabo Curioso (Fig. 15) suggests a composite history: first, extended seafloor

reworking demonstrated by chemically evolved glaucony and reworked skeletal material; second, a second phase of reworking, but one related to more rapid burial as defined by less chemically evolved glaucony in the overlying Monte León Formation. If our interpretation is correct, then (1) this unit forms a coarse-grained ravinement deposit, with absence in the Playa La Mina section illustrating only local development (Fig. 4, 15); and (2) the interpreted unconformity separating the two formations may not represent a substantial amount of time.

6.2. Siderite formation associated with marine transgression

Siderite, whether *in situ* or reworked in rock clasts, is stratigraphically restricted to strata within 1 m above the ravinement surface in the upper Gran Bajo Member (Fig. 15). This suggests that its formation is related to geochemical conditions generated with the change from marginal to fully marine conditions during transgression. Siderite precipitates in sub-oxic or strongly reducing conditions (Bernier, 1971; Froelich et al., 1979). Elevated $\delta^{13}\text{C}$ (–6, +11‰) and slightly negative $\delta^{18}\text{O}$ values (–3.6, –3.5‰; Supplemental Table 4) identify, respectively, likely involvement of (1) bacterially mediated methanogenesis (Irwin et al., 1977) during (2) mixing of meteoric and marine waters (Mozley and Wersin, 1992). Differences in the accessory grain types in these siderites (i.e., phytoliths versus cryptocrystalline grains) define lateral facies variation along the coastal setting. The depositional framework discussed here is similar to the origin of siderite in Eocene coastal-plain deposits of New Zealand, also reworked by late Oligocene marine transgression (Middleton and Nelson, 1996).

MARINE-DERIVED



BURIAL

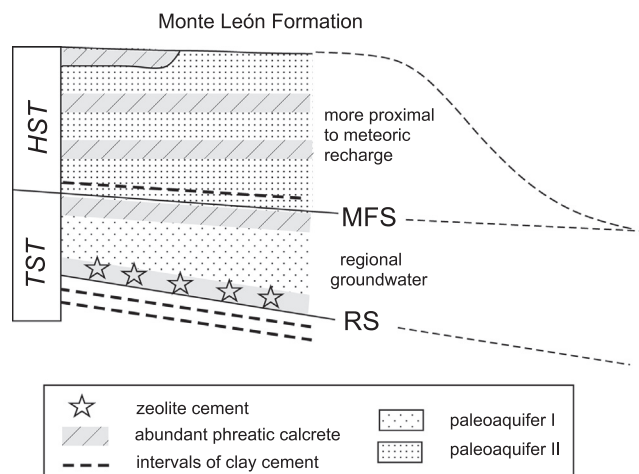


Fig. 15. Schematic illustration (not to scale) showing general stratigraphic patterns of marine-derived and burial diagenetic attributes, and interpreted distinct paleoquifers, with respect to sequence stratigraphy of the San Julián Formation. The seaward extensions of system tracts and seaward limit of the highstand system tract are shown as reference. Abbreviations: TST, transgressive system tract; MFS, maximum flooding surface; HST, highstand system tract; RS, ravinement surface; RS_{local}, local ravinement surface.

6.3. Maximum flooding surface: cool-water incursion in a warm-water setting

Biofacies of the San Julián Formation identifies a relatively warm-water, shallow shelf-interior (Barreda, 1997; Parras and Casadío, 2005; Erdmann et al., 2008; Nández et al., 2009). Our study reinforces this through the discovery of micrite in all the oyster-dominated skeletal rudstones. Micrite is commonly associated with warm-water carbonate systems (Bathurst, 1975) and only rarely occurs in temperate latitude platforms (Smith and Nelson, 2003). It is usually most abundant where input of siliciclastics is much reduced (Bathurst, 1975). There is no texture or fabric in our sections that clearly distinguishes a detrital (i.e., transported) from authigenic (in situ) origin (Tucker and Wright, 1990; Riding, 2000). It remains uncertain whether the filigree fabric (Fig. 12B, E) is an artifact of microspar replacement or might identify relict microbial structure (Riding, 2000). Restriction of micrite to shelter porosity, together with the contemporary authigenesis of evolved glaucony (see above), suggests that carbonate production occurred in

a protected microenvironment coincident with or following extended seafloor reworking and reduced siliciclastic accumulation.

Stratigraphically constrained textural and geochemical data suggest that incursions of cooler water occurred within this warm-water setting. Microfibrillar isopachous cement (Fig. 11A–B) is texturally similar to interpreted magnesian calcite cement reported from an upper Oligocene cool-water carbonate platform in New Zealand (Nelson and James, 2000). In the San Julián Formation, textural gradation from microfibrillar to inclusion-rich and -poor microsparite suggests that equivalent microsparite is a diagenetic alteration of this original cement, highly mineralogical metastability. The cement occurs along and beneath the maximum flooding surface, a paleosurface that usually defines maximum water depth related to transgression (Handford and Loucks, 1993; Catuneanu, 2006), and, for this particular example, a shift to below fair-weather wave base (Parras and Casadío, 2005). As the cement is also found in the glauconitic oyster-dominated skeletal rudstones of the highstand succession (Fig. 15), this suggests that these skeletal concentrations may incorporate a history of extended marine exposure related to base level change.

Supporting evidence for a cooler-water setting along the maximum flooding surface is provided by the $\delta^{18}\text{O}$ composition of brachiopod calcite. As this paleosurface records a more offshore paleoenvironment (Parras and Casadío, 2005), brachiopod calcite serves as a proxy for more open-shelf seawater chemistry (James et al., 1997). The linear trend in $\delta^{13}\text{C}$ values defined by all our brachiopod samples extends away from the expected marine composition (Fig. 14A). This likely records differential mixing of more depleted ^{13}C associated with diagenetic calcite that fills shell punctae. A similar trend occurs in equivalent marine strata in Australia (Pufahl et al., 2006). The least-influenced skeletal composition of our dataset, falling within the marine field, corresponds to a sample from beneath the maximum flooding surface (Fig. 14A).

A temperature estimate of 11–13 °C is calculated based on the fractionation equation published by O'Neil et al. (1969), and a coastal marine $\delta^{18}\text{O}_{\text{seawater}}$ value of ~ -0.5 to -0.8 for the late Oligocene that is similar to contemporary Southern Ocean seawater (Paul et al., 2000). A similar temperature estimate was reported by Nelson et al. (1983) for equivalent (Chattian; late Oligocene) cool-water open shelf oyster biofacies in New Zealand. For this paleoceanographic setting, Nelson and James (2000) interpreted sea-level lowstands as being important for warming the seafloor and increasing saturation states that promoted magnesian calcite, but not aragonite, cement. In the Austral Basin, the reverse has likely occurred: incursion of open-shelf waters related to short-term sea-level rise cooled an otherwise warm seafloor. Locally etched skeletal surfaces overlain by the interpreted cooler water marine cement (Fig. 11C) may be evidence of corrosion related to exchange of cool for warmer waters.

6.4. Stratigraphically constrained burial cements

Zeolite, clay, and carbonate cements (exclusive of the microfibrillar calcite) are of burial origin, post-dating mechanical compaction that produced point and long intergrain contacts. Calcite is the predominant cement type, with the following facies and stratigraphically bound exceptions. First, the restriction of burial zeolite (clinoptilolite-K) cement (Fig. 9B) to sediment above (<1 m) the ravinement surface (Fig. 15) in the Gran Bajo Member suggests that an initial elevated activity ratio ($\text{Na}^+ + \text{K}^+ + \text{Ca}^{2+} / \text{H}^+$) (Hay and Sheppard, 2001), may have been related to metastability of weathered silicates reworked from the coastal-plain deposits. With ongoing transgression, this stratigraphically overstepped depositional source was no longer available. Subsequent rare zeolite is associated with or follows late-stage Fe-oxidation (Fig. 9D, 11D). Second, the restriction of clay (illite) cement to siliciclastic-rich facies (Fig. 15) suggests that detrital (skeletal) carbonate normally formed a sufficient buffer for pore-water pH. In its absence, acidic pore-water would promote formation of authigenic clay (Hay and Sheppard, 2001).

6.5. Geochemical segregation of carbonate phreatic diagenesis

Microsparite and bladed to equant crystalline calcite cements (Fig. 8) occupy most of the paleoporosity in oyster-dominated skeletal rudstones. Negative displacement of their stable carbon and oxygen isotope values from the expected marine field (Fig. 14A) supports precipitation from meteoric fluids but differentially influenced from a source depleted in ^{13}C (Lohmann, 1988). Gradational textural boundaries between micrite and microsparite (Fig. 12) identify progressive recrystallization of micrite, or neomorphism (Folk, 1965). This has produced the patchy to locally wholesale masses of microsparite (Fig. 12). As microsparite and microfibrillar calcite cement are always overlain by later calcite cements, alteration of micrite and marine cement likely occurred during influx of meteoric fluids. As these cements post-date completion of mechanical compaction, occlusion of most of the paleoporosity related to skeletal rudstones is of burial origin.

Textural attributes associated with recrystallization of micrite to microsparite, and occlusion of available porosity by cement, characterize attributes of endmember alpha- and beta phreatic calcrete lithotypes (Tucker and Wright, 1990; Durand et al., 2010). This includes: microcrystalline peloidal or pseudopeloid texture; etched silicate grains; skeletal paleomolds filled with later calcite cement; sand-size carbonate and silicate grains dispersed in a microcrystalline mosaic; silicate-grain paleomolds; and, circum-granular and other paleocracks filled with calcite cement. The once very porous skeletal rudstones were transformed into stratigraphically restricted thin (<1.5 m) layers of phreatic calcrete (Fig. 15).

Trace element (Sr, Na) concentrations suggest differences in water–rock interaction related to each depositional system tract. Sr concentrations from paleomold and shelter-porosity cements, and altered (once aragonitic) bivalve shells, fall within the expected range (1000–4000 ppm; Fig. 13A, B) of unaltered aragonitic bivalves and gastropods (Table 4; Morse and Mackenzie, 1990). In fact, the host mixed sediment contains a variety of Sr sources that may have contributed (Table 4). Partial to complete geochemical inheritance during diagenesis reflects incomplete removal of trace elements by water flow, and is a characteristic of a relatively closed system. In Playa La Mina, Na values in some diagenetic carbonate lie above the 1:1 diagenetic ratio that forms the upper limit of diagenetic carbonate from Quaternary carbonate systems (Fig. 13C). Such elevated values also suggest geochemical inheritance, with Na incorporated from either saline pore-water or Na adsorbed onto siliciclastic particles.

The covariance in $\delta^{13}\text{C}$ and $\delta^{18}\text{O}$ values in the highstand succession at Playa La Mina (Fig. 13B) may also be interpreted in terms of a hydrologically closed system (Li and Ku, 1997). In this case, covariant negative shifts in both isotope ratios would record greater throughput of meteoric-derived waters, whereas positive shifts define either

reduced meteoric throughput and greater inheritance of marine signatures, or more evaporative pore water (Li and Ku, 1997). The upsection isotope-ratio increase in the highstand succession, in contrast to an invariant profile for Cabo Curioso, suggests that there was either vertical mixing with more evaporated pore water moving downsection, or greater geochemical inheritance (Lohmann, 1988). The potential role of elevated salinity is supported by paleocracks in microsparite (Fig. 12B, F) that are similar to those related to salinity changes affecting organic matter and clay interred within micritic microbial sediment (Harazim et al., 2013).

From the transgressive system tract, the tight $\delta^{18}\text{O}$ – $\delta^{13}\text{C}$ data cluster well removed from a marine signature (Fig. 14A) is an expected product of phreatic diagenesis occurring distal to a meteoric recharge zone, where $\delta^{13}\text{C}$ values mimic the host carbonate rock (Morse and Mackenzie, 1990). The clustered values lie along a burial meteoric pathway defined from Upper Oligocene cool-water limestone in New Zealand (Fig. 14A; Dix and Nelson, 2006). In comparison, the more positive, dispersed, array of $\delta^{18}\text{O}$ values in the highstand systems tract coupled with a heterogeneous distribution of negative (–4 to –12‰) $\delta^{13}\text{C}$ values illustrate either greater proximity to meteoric recharge, with strong influence of soil–gas derived bicarbonate (Allan and Matthews, 1982; Morse and Mackenzie, 1990) or involvement of *in situ* bacterially mediated sulfate reduction (Irwin et al., 1977).

The covariant negative shift in isotope ratios immediately beneath the Monte León Formation (Fig. 14B), therefore, could be interpreted as evidence for subaerial exposure, with soil-derived bicarbonate being depleted in ^{13}C (Allan and Matthews, 1982). However, there is no textural evidence for subaerial exposure. Alternatively, the negative excursion in both isotope values may only identify greater meteoric throughput specific to this coarser-grained unit.

6.6. The significance of integrated diagenetic and sequence stratigraphies

The transgressive-highstand system tract of the San Julián Formation thins (~30 m) northeastward over a distance of ~30 km from the Gran Bajo to present-day coastal sections (Fig. 1B). Yet, over this distance, there is no significant lateral change in water depth as defined by depositional facies (Manassero et al., 1997; Parras and Casadío, 2005). The coastal sections, therefore, are stratigraphically condensed.

We interpret the change in thickness change to record differential basement subsidence over the minimum distance of 30 km. The San Julián Formation overlies the southwest margin of the Deseado Massif, which also formed a landmass to the north in the latest Oligocene–early Miocene (Fig. 1A). Outcrop and subsurface data show that this entire region, including the study area, is underlain by a Permian–Triassic rift basin (Homoc and Constantini, 2001). In a foreland basin, a regional mosaic of differential subsidence arising from loading along the orogen may emerge according to inherited basement structure (Jordan, 1995). Progressive eastward movement of retroarc deformation related to contractional orogenic events (Thomson et al., 2001) would form a driver of regional subsidence across the Austral Basin, modified locally by differential basement reactivation. Relative uplift along the massif or increased subsidence along the southwestern structural limit therefore could explain SW-directed thickening of the marine transgressive-highstand system tract succession.

However, the period of sediment accumulation extending from the maximum flooding surface through to the top of the highstand system tract appears to fit, based on Sr-isotope data, with global sea-level highstand extending through the late Oligocene–early Miocene period (Fig. 3B). This suggests a period of both tectonic and eustatic influences at this locality in this retroarc foreland basin. The interpreted incursion of cooler water along the maximum flooding surface, possibly promoting seafloor cement, is a herald of later regional transgression defined by the Monte León Formation in the early Miocene. Within the highstand succession, the occurrence of chemically-evolved glaucony and similar marine cement with oyster-dominated event deposits

Table 4
Potential sources of Sr^a.

	Sr (ppm)
Aragonite	
Gastropod	2000
Bivalves	1000–4000
Micrite	8000
Calcite (+ Mg)	
Micrite	1200
Barnacles	2800–4000 (Bourget, 1974)
Bryozoans	2000–2500
Echinoids	2000
Volcanics	
Basalt ^b	413 (D'Ozario et al., 2004)
Andesite	601 (regional Andean: Bailey, 1981)
Felsic ^c	80–220 (Páez et al., 2010)

^a Morse and Mackenzie (1990) except where noted.

^b Deseado Massif: plateau basalt (Paleogene–Neogene).

^c Jurassic Bahia Laura Group (Deseado Massif).

(Fig. 15) may also suggest prominent paleoceanographic change controlled by higher order base level changes. In siliciclastic-bearing platforms, a slight rise in sea level will sequester sand-size siliciclastics along the coastal zone (Catuneanu, 2006). But, in a mixed sediment environment, reduced rates of accumulation offshore will increase the extent of seafloor reworking, promote carbonate accumulation, and enhance the potential that skeletal concentration deposits will be greatly affected by episodic storm events (Parras and Casadío, 2005). Whether these possible base level changes were a response to contemporary higher-order Antarctic-based glaciations (Webb and Strong, 2006) or subtle changes in basement subsidence (see above) is unknown.

The mismatch between renewed transgression defined by the base of the Monte León Formation and the decrease in global sea level that follows the San Julián highstand succession (Fig. 3B) may be a product of increased subsidence due to regional structural loading along the margin of the foreland basin (Jordan, 1995). Absence of obvious vadose diagenetic textures in the uppermost San Julián Formation, coupled with admixture of differentially evolved glauconies in this same unit, suggest that meteoric diagenesis likely evolved contemporaneously with later basin emergence by the early to middle Miocene. Fe-oxidation, much of which overprints the San Julián Formation, may be a record of increasing aridity with continental deposition at this time.

Texturally, the marine transgressive-highstand system tract succession of the San Julián Formation would have formed a regional confined paleoaquifer bound by finer grained coastal-plain deposits of the lower transgressive succession in the Gran Bajo Member, and the overlying muddy siliciclastic facies of the Monte León Formation (Fig. 15). Within this regional unit, however, geochemistry of the transgressive and highstand system tracts from the coastal sections (Fig. 14) delimit the system tracts themselves as distinct paleoaquifers, separated by the maximum flooding surface (Fig. 15). Accommodating the minor change in $\delta^{18}\text{O}$ of ocean water in the south Atlantic since the late Oligocene (Schmidt et al., 1999; Paul et al., 2000), calcites in the transgressive system tract have $\delta^{18}\text{O}$ values similar to a calcite if precipitated from regional Quaternary groundwater in Patagonia (Fig. 14A; Mayr et al., 2012). In contrast, calcites in the highstand succession are compositionally similar to calcites if precipitated from groundwater fed by coastal rainfall along Patagonia (Fig. 14A; Mayr et al., 2012). This comparison supports our interpretation that burial diagenesis in the transgressive system tract was distal to and within a regional paleoaquifer system whereas the more varied geochemical environment of the highstand system tract (characterizing differential rock–water interaction and possibly salinity) may identify a stratigraphic position more proximal to meteoric recharge (Fig. 15).

7. Conclusions

In the upper Oligocene–lower Miocene San Julián Formation, diagenetic silicates and calcite textures are spatially organized within a condensed (~20 m thick) marine transgressive-highstand system tract succession. Using integrated diagenetic and sequence stratigraphic analysis, the highstand succession appears to be a record of eustatic control, whereas a regional increase in its thickness away from an area of stratal condensation is a record of differing rates of subsidence.

Marine transgression across marginal-marine coastal-plain deposits produced transient mixing of meteoric and marine fluids resulting in formation of depositional siderite. Marine-derived diagenetic attributes (chemically-evolved glaucony, magnesian calcite marine cement) in the marine transgressive and highstand system tracts are restricted to strata within which facies define prominent seafloor reworking or extended marine exposure. Less chemically evolved glaucony is associated with more rapid burial associated with renewed transgression across the top of the formation. Seafloor cement, possibly once magnesian calcite, is well developed along the maximum flooding surface and coincided with incursion of cool (~11–13 °C) seawater. Its presence in skeletal

event beds in the highstand succession suggests that these also record sea-level rise.

In the burial realm, phreatic meteoric diagenesis is pervasive, and forms resistant layers of phreatic calcrete where paleoporosity was abundant. Two exceptions to this are facies-defined: first, intergranular zeolite (clinoptilolite-K) cement is restricted to strata related to initial marine transgression, likely a record of elevated pore-water activity due to initial metastability of reworked coastal-plain silicates; and, second, clay (illite) cement occurs in a few siliciclastic-rich intervals likely where a limited supply of skeletal carbonate failed to buffer pore-water pH. Trace element and stable (C, O) isotope geochemistry of carbonate diagenesis identify two paleoaquifer systems: (1) the marine transgressive system tract, in which diagenesis was distal to meteoric recharge and part of a regional paleoaquifer; and (2) the highstand system tract, which may have been more proximal to a meteoric recharge source; was more influenced from a bicarbonate source depleted in ^{13}C ; and, displays more variable rock–water interaction and/or salinities.

Acknowledgments

This study was supported by Canadian and Argentine research grants: a Natural Sciences and Engineering Research Council Discovery Grant to G.R. Dix; and, CONICET (PIP11420080100503) and SECyT (PI188 FCEyN-UNLPam) grants to A. Parras. We thank M. Griffin, Javier Signorelli, and Diego Urteaga for assistance in the field. We thank Peter Jones (microprobe) and J.J. (SEM) for their analytical expertise. Two anonymous journal reviewers are thanked for their comments that improved the original manuscript.

Appendix A. Supplementary data

Supplementary data to this article can be found online at <http://dx.doi.org/10.1016/j.sedgeo.2014.04.003>.

References

- Allan, J.R., Matthews, R.K., 1982. Isotope signatures associated with early meteoric diagenesis. *Sedimentology* 29, 797–817.
- Amorosi, A., 1995. Glaucony and sequence stratigraphy: conceptual framework of distribution in siliciclastic sequences. *Journal of Sedimentary Research* B65, 419–425.
- Amorosi, A., 1997. Detecting composition, spatial, and temporal attributes of glaucony: a tool for provenance study. *Sedimentary Geology* 109, 135–153.
- Armbruster, T., 2001. Clinoptilolite–heulandite: applications and basic research. In: Galarnau, A., Di Renzo, F., Faujula, F., Vedrine, J. (Eds.), *Zeolites and Mesoporous Materials at the Dawn of the 21st Century*. Elsevier Science, pp. 13–27.
- Bailey, J.C., 1981. Geochemical criteria for a refined tectonic discrimination of orogenic andesites. *Chemical Geology* 32, 139–154.
- Barreda, V.D., 1997. Palinoestratigrafía de la Formación San Julián en el área de Playa La Mina (provincia de Santa Cruz), Oligoceno de la cuenca Austral. *Ameghiniana* 34, 283–294.
- Barreda, V., Palazzesi, L., Marensi, S., 2009. Palynological record of the Paleogene Río Leona Formation (southernmost South America): stratigraphical and paleoenvironmental implications. *Review of Palaeobotany and Palynology* 154, 22–33.
- Bathurst, R.G.C., 1975. *Carbonate Sediments and Their Diagenesis*. Elsevier, Amsterdam (658 pp.).
- Bertels, A., 1970. Sobre el “Piso Patagónico” y la representación de la época del Oligoceno en Patagonia austral, República Argentina. *Revista de la Asociación Geológica Argentina* 25, 495–501.
- Berner, R.A., 1971. *Principles of Chemical Sedimentology*. McGraw-Hill, New York (240 pp.).
- Bourget, E., 1974. Environmental and structural control of trace elements in barnacle shells. *Marine Biology* 28, 27–36.
- Buckley, H.A., Easton, A.J., Johnson, L.R., 1984. Compositional variations in glauconite. *Mineralogical Magazine* 48, 119–126.
- Burst, J.F., 1958. Mineral heterogeneity in “glauconite” pellets. *American Mineralogist* 43, 481–497.
- Carriker, M.R., Swann, C.P., Prezant, R.S., Counts III, C.L., 1991. Chemical elements in the aragonitic and calcitic microstructural groups of shell of the oyster *Crassostrea virginica*: a proton probe study. *Marine Biology* 109, 287–297.
- Carriker, M.R., Swann, C.P., Ewart, J., Counts III, C.L., 1996. Ontogenetic trends of elements (Na to Sr) in prismatic shells of living *Crassostrea virginica* (Gmelin) grown in three ecologically dissimilar habitats for 28 weeks: a proton probe study. *Journal of Experimental Marine Biology and Ecology* 201, 87–135.
- Catuneanu, O., 2006. *Principles of Sequence Stratigraphy*. Elsevier, Amsterdam (386 pp.).

- Chafetz, H., Reid, 2000. Syndepositional shallow-water precipitation of glauconitic minerals. *Sedimentary Geology* 136, 29–42.
- Deines, P., Langmuir, D., Harmon, R.S., 1974. Stable carbon isotope ratios and the existence of a gas phase in the evolution of carbonate ground waters. *Geochimica et Cosmochimica Acta* 38, 1147–1164.
- Dix, G.R., Nelson, C.S., 2006. Diagenetic potential for lithification of cool-water carbonate shelf mud. *Sedimentary Geology* 185, 41–58.
- Dott Jr., R.H., 1964. Wacke, greywacke and matrix – what approach to immature sandstone classification? *Journal of Sedimentary Petrology* 34, 625–632.
- D'Ozario, M., Innocenti, F., Manetti, P., Haller, M.J., 2004. Cenozoic back-arc magmatism of the southern extra-Andean Patagonia (44° 30' – 52° S): A review of geochemical data and geodynamic interpretations. *Revista de la Asociación Geológica Argentina* 59, 525–538.
- Durand, N., Monger, H.C., Canti, M., 2010. Calcium carbonate features. In: Marcelino, V., Mees, F. (Eds.), *Stoops, G. Interpretation of Micromorphological Features of Soils and Regoliths*, Elsevier, Amsterdam, pp. 149–193.
- Eder, V.G., Martín-Algarra, A., Sánchez-Navas, A., Zanin, Y.N., Zamirailova, A.G., Lebedev, Y. N., 2007. Depositional controls on glaucony texture and composition, Upper Jurassic, West Siberian Basin. *Sedimentology* 54, 1365–1387.
- Embry, A.F., Klován, J.E., 1971. A late Devonian reef tract on northeastern Banks Island, Northwest Territories. *Bulletin of Canadian Petroleum Geology* 19, 730–781.
- Erdmann, S., Bellosi, E.S., Morra, G.A., 2008. Una nueva especie de coral solitario (*Scleractinia*, *Turbinoliidae*) de la Formación San Julián (Oligoceno superior, Santa Cruz) en su contexto estratigráfico y paleoambiental. *Revista del Museo Argentino de Ciencias Naturales* 10, 255–262.
- Feagle, J.G., Bown, T.M., Swisher, C., Buckley, G., 1995. Age of the Pinturas and Santa Cruz Formations. *Actas 6° Congreso Argentino de Paleontología y Bioestratigrafía* 129–135 (Trewel).
- Folguera, A., Ramos, V.A., 2011. Repeated eastward shifts of arc magmatism in the Southern Andes: a revision to the long-term pattern of Andean uplift and magmatism. *Journal of South American Earth Sciences* 32, 531–546.
- Folk, R.L., 1965. Some aspects of recrystallization in ancient limestones. In: Pray, L.C., Murray, R.C. (Eds.), *Dolomitization and Limestone Diagenesis*. Society of Economic and Paleontological Mineralogists Special Publication, 13, pp. 14–48.
- Froelich, P.N., Klinkhammer, G.P., Bender, M.L., Luedtke, N.A., Heath, G.R., Cullen, D., Dauphin, P., 1979. Early oxidation of organic matter in pelagic sediments of the eastern equatorial Atlantic: suboxic diagenesis. *Geochimica et Cosmochimica Acta* 43, 1075–1090.
- Guido, D.M., Escayola, M.P., y Schalamuk, I.B., 2004. The basement of the Deseado Massif at Bahía Laura, Patagonia, Argentina: a proposal for its evolution. *Journal of South American Earth Sciences* 16, 567–577.
- Handford, C.R., Loucks, R.G., 1993. Carbonate depositional sequences and systems tracts – responses of carbonate platforms to relative sea-level changes. In: Loucks, R.G., Sarg, J.F. (Eds.), *Carbonate Sequence Stratigraphy: Recent Advances and Applications*. American Association of Petroleum Geologists Memoir, 57, pp. 3–41.
- Harazim, D., Callow, R.H.T., McIroy, D., 2013. Microbial mats implicated in the generation of intratratral shrinkage ('synaeresis') cracks. *Sedimentology* 60, 1–18.
- Hay, R.L., Sheppard, R.A., 2001. Occurrence of zeolites in sedimentary rocks: an overview. In: Bish, D.L., Ming, D.W. (Eds.), *Natural Zeolites: Occurrence, Properties, Applications*. Reviews in Mineralogy and Geochemistry, 45, pp. 217–234.
- Hendricks, S.B., Ross, C.S., 1941. Chemical composition and genesis of glauconite and celadonite. *American Mineralogist* 26, 683–708.
- Hesselbo, S.P., Huggett, J.M., 2001. Glaucony in ocean-margin sequence stratigraphy (Oligocene–Pliocene, offshore New Jersey, USA; ODP Leg 174). *Journal of Sedimentary Research* 71, 599–607.
- Homovc, J.F., Constantini, L., 2001. Hydrocarbon exploration potential within intraplate shear-related depocenters: Deseado and San Julián basins, southern Argentina. *American Association of Petroleum Geologists Bulletin* 85, 1795–1816.
- Iglesias, A., Artabe, A.E., Morel, E.M., 2011. The evolution of Patagonian climate and vegetation from the Mesozoic to the present. *Biological Journal of the Linnean Society* 103, 409–422.
- Ireland, B.J., Curtis, C.D., Whiteman, J.A., 1983. Compositional variation within some glauconites and illites and implications for their stability and origins. *Sedimentology* 30, 769–786.
- Irwin, H., Curtis, C., Coleman, M., 1977. Isotopic evidence for source of diagenetic carbonates formed during burial of organic-rich sediments. *Nature* 269, 209–213.
- James, N.P., Bone, Y., Kyser, T.K., 1997. Brachiopod $\delta^{18}\text{O}$ values do reflect ambient oceanography: Lacedpede Shelf, southern Australia. *Geology* 25, 551–554.
- Jordan, T.E., 1995. Retroarc foreland and related basins. In: Busby, C.J., Ingersoll, R.V. (Eds.), *Tectonics of Sedimentary Basins*. Blackwell Science, London, pp. 331–362.
- Kominz, M.A., Browning, J.V., Miller, K.G., Sugarman, P.J., Mizintseva, S., Scotese, C.R., 2008. Late Cretaceous to Miocene sea-level estimates from the New Jersey and Delaware coastal plain coreholes: an error analysis. *Basin Research* 20, 211–226.
- Kyser, T.K., James, N.P., Bone, Y.B., 1998. Alteration of Cenozoic cool-water carbonates to low-Mg calcite in marine waters, Gambier Embayment, South Australia. *Journal of Sedimentary Research* 68, 947–955.
- Land, L.L., Hoops, G.K., 1973. Sodium in carbonate sediments and rocks: a possible index to the salinity of diagenetic solutions. *Journal of Sedimentary Petrology* 43, 614–617.
- Li, H.C., Ku, T.L., 1997. $\delta^{13}\text{C}$ – $\delta^{18}\text{O}$ covariance as a paleohydrological indicator for closed-basin lakes. *Palaeogeography, Palaeoclimatology, Palaeoecology* 133, 69–80.
- Lohmann, K.C., 1988. Geochemical patterns of meteoric diagenetic systems and their application to studies of paleokarst. In: James, N.P., Choquette, P.W. (Eds.), *Paleokarst*. Springer-Verlag, pp. 58–80.
- Longuépée, H., Cousineau, P.A., 2006. Constraints on the genesis of ferric illites and aluminum-rich glauconite: potential impact on sedimentology and isotopic studies. *Canadian Mineralogist* 44, 967–980.
- Lu, F.H., 2008. Pristine or altered: low-Mg calcite shells survived from massive dolomitization? A case study from Miocene carbonates. *Geo-Marine Letters* 28, 339–349.
- MacMillan, L.C., 2010. Comparative sedimentology and paleoecology of fossil giant oyster beds in some Tertiary strata of New Zealand and Argentina. (MSc Thesis) University of Waikato (300 pp.).
- Madella, M., Alexandre, A., Ball, T., 2005. International code for phytolith nomenclature 1. 0. *Annals of Botany* 96, 253–260.
- Malumián, N., Nández, C., 2011. The Late Cretaceous–Cenozoic transgressions in Patagonia and the Fuegian Andes: foraminifera, palaeoecology and palaeogeography. *Biological Journal of the Linnean Society* 103, 269–288.
- Manassero, M., Griffin, M., Pastorino, G., 1997. Coquinas and shelf deposits of the San Julián Formation (Upper Eocene–Lower Oligocene) southern Patagonia, Argentina. *Revista de la Asociación Geológica Argentina* 52, 286–296.
- Mayr, C., Lucke, A., Stichler, W., Trimborn, P., Ercolano, B., Oliva, G., Ohlendorf, C., Soto, J., Fey, M., Haberzettl, Janssen, S., Schabitz, F., Schieser, G.H., Wille, M., Zolitschka, 2012. Precipitation origin and evaporation of lakes in semi-arid Patagonia (Argentina) inferred from stable isotopes ($\delta^{18}\text{O}$, $\delta^2\text{H}$). *Journal of Hydrology* 334, 53–63.
- Matheos, S.D., Raigemborn, M.S., 2012. Sedimentology and paleoenvironment of the Santa Cruz Formation. In: Vizcaíno, S.F., Kay, R.F., Bargo, M.S. (Eds.), *Early Miocene Paleobiology in Patagonia: High Latitude Paleocommunities of the Santa Cruz Formation*. Cambridge University Press, Cambridge, pp. 59–82.
- Middleton, H.A., Nelson, C.S., 1996. Origin and timing of siderite and calcite concretions in late Palaeogene non- to marginal-marine facies of the Te Kuiti Group, New Zealand. *Sedimentary Geology* 103, 93–115.
- Morad, S., Ketzer, J.M., De Ros, L.F. (Eds.), 2012. *Linking Diagenesis to Sequence Stratigraphy*. 45. International Association of Sedimentologists Special Publication.
- Morbidelli, P., Rosaria Ghiara, M., Lonis, R., Petti, C., 2001. Quantitative distribution and chemical composition of authigenic clinoptilolite-bearing ignimbrites from northern Sardinia (Italy): inferences for mineralogical models. *Periodico di Mineralogia* 70, 71–97.
- Morse, J.W., Mackenzie, F.T., 1990. *Geochemistry of Sedimentary Carbonates*. Elsevier, Amsterdam (707 pp.).
- Mount, J.F., 1984. Mixing of siliciclastic and carbonate sediments in shallow shelf environments. *Geology* 12, 432–435.
- Mozley, P.S., Wersin, P., 1992. Isotopic composition of siderite as an indicator of depositional environment. *Geology* 20, 817–820.
- Nández, C., Quattrocchio, M.E., Ruiz, L., 2009. Palinología y micropaleontología de las Formaciones San Julián y Monte León (Oligoceno–Mioceno temprano) en el subsuelo de cabo Curioso, provincia de Santa Cruz, Argentina. *Ameghiniana* 46, 669–693.
- Nelson, C.S., James, N.P., 2000. Marine cements in mid-Tertiary cool-water shelf limestones of New Zealand and southern Australia. *Sedimentology* 47, 609–629.
- Nelson, C.S., Burns, D.A., Rodgers, K.A., 1983. The taxonomic status, and isotopic evidence for paleoenvironments of giant oysters from Oligocene Te Kuiti Group, South Auckland, New Zealand. *New Zealand Journal of Geology and Geophysics* 26, 289–299.
- Odin, G.S., Matter, A., 1981. De glauconiarum origine. *Sedimentology* 28, 611–641.
- Ogihara, S., 2000. Composition of clinoptilolite formed from volcanic glass during burial diagenesis. *Clays and Clay Minerals* 48, 106–110.
- O'Neil, J.R., Clayton, R.N., Mayeda, T.K., 1969. Oxygen isotope fractionation in divalent metal carbonates. *Journal of Chemical Physics* 51, 5547–5558.
- Oscarson, R.L., Bargar, K.E., 1996. Electron microprobe analyses of zeolite minerals from Neogene volcanic rocks in the Breitenbush–Austin Hot Springs area, Oregon. USGS Open File Report. US Geological Survey, Menlo Park, Ca, pp. 41–96.
- Páez, G.N., Ruiz, R., Guido, D.M., Jovic, S.M., Schalamuk, I.B., 2010. The effects of K-metasomatism in the Bahía Laura Volcanic Complex, Deseado Massif, Argentina: petrologic and metallogenic consequences. *Chemical Geology* 273, 300–313.
- Parras, A., Casadio, S., 2005. Taphonomy and sequence stratigraphic significance of oyster-dominated concentrations from the San Julián formation, Oligocene of Patagonia, Argentina. *Palaeogeography, Palaeoclimatology, Palaeoecology* 217, 47–66.
- Parras, A., Casadio, S., 2006. The oyster *Crassostrea? hatcheri* (Ortmann, 1897), a physical ecosystem engineer from the Upper Oligocene–Lower Miocene of Patagonia, southern Argentina. *Palaos* 21, 168–186.
- Parras, A., Griffin, M., Feldmann, R., Casadio, S., Schweitzer, C., Marenssi, S., 2008. Correlation of marine beds based on Sr- and Ar-date determinations and faunal affinities across the Paleogene/Neogene boundary in southern Patagonia, Argentina. *Journal of South American Earth Sciences* 26, 204–216.
- Parras, A., Griffin, M., 2009. Darwin's Great Patagonian Tertiary Formation at the mouth of the Rio Santa Cruz: a reappraisal. *Revista de la Asociación Geológica Argentina* 64, 70–82.
- Parras, A., Dix, G.R., Griffin, M., 2012. Sr-isotope chronostratigraphy of Paleogene–Neogene marine deposits: Austral Basin, southern Patagonia (Argentina). *Journal of South American Earth Sciences* 37, 122–135.
- Paul, H.A., Zachos, J.C., Flower, B.P., Tripathi, A., 2000. Orbitally induced climate and geochemical variability across the Oligocene/Miocene boundary. *Paleoceanography* 15, 471–485.
- Porrenga, D.H., 1967. Glauconite and chamosite as depth indicators in the marine environment. *Marine Geology* 5, 495–501.
- Pufahl, P.K., James, N.P., Kyser, T.K., Lukasik, J., Bone, Y., 2006. Brachiopods in epeiric seas as monitors of secular changes in ocean chemistry: a Miocene example from the Murray Basin, South Australia. *Journal of Sedimentary Research* 76, 926–941.
- Riding, R., 2000. Microbial carbonates: the geological record of calcified bacterial–algal mats and biofilms. *Sedimentology* 47 (Supplement 1), 179–214.
- Russo, A., Flores, M.A., Di Benedetto, H., 1980. Patagonia austral extraandina. In: Turner, J. C.M. (Ed.), *Segundo Simposio de Geología Regional Argentina*. Academia Nacional de Ciencias, Córdoba, Argentina, pp. 1431–1462.

- Sánchez-Navas, A., Martín-Algarra, A., Eder, V., Reddy, B.J., Nieto, F., Zanin, Y.N., 2008. Color, mineralogy, and composition of Upper Jurassic West Siberian Glauconite: useful indicators of paleoenvironment. *Canadian Mineralogist* 46, 1545–1564.
- Scher, H.D., Martin, E.E., 2006. Timing and climatic consequences of the opening of Drake Passage. *Science* 312, 428–430.
- Schmidt, G.A., Bigg, G.R., Rohling, E.J., 1999. Global Seawater Oxygen-18 Database – v1.21. <http://data.giss.nasa.gov/o18data> (access online:).
- Smith, A.M., Nelson, C.S., 2003. Effects of early sea-floor processes on the taphonomy of temperate shelf skeletal carbonate deposits. *Earth-Science Reviews* 63, 1–31.
- Suárez, M., de la Cruz, R., Bell, C.M., 2000. Timing and origin of deformation of the Patagonian fold and thrust belt. *Geological Magazine* 137, 345–353.
- Taylor, K.G., Gawthorpe, R.L., Curtis, C.D., Marshall, J.D., Awwiller, D.N., 2000. Carbonate cementation in a sequence stratigraphic framework: Upper Cretaceous sandstones, Book Cliffs, Utah–Colorado. *Journal of Sedimentary Research* 70, 360–372.
- Takahashi, J.-I., 1939. Synopsis of glauconitization. In: Trask, P.K. (Ed.), *Recent Marine Sediments: A Symposium*. American Association of Petroleum Geologists, pp. 503–512 (Tulsa).
- The Geologic Time Scale 2012. In: Gradstein, F.M., Ogg, J.G., Schmitz, M.D., Ogg, G.M. (Eds.), Elsevier, Amsterdam (1144 pp.).
- Thomson, S.N., Herve, F., Stockhert, B., 2001. Mesozoic–Cenozoic denudation history of the Patagonian Andes (southern Chile) and its correlation to different subduction processes. *Tectonics* 20, 693–711.
- Tucker, M.E., 1993. Carbonate diagenesis and sequence stratigraphy. In: Wright, V.P. (Ed.), *Sedimentology Review* 1, pp. 51–72.
- Tucker, M.E., Wright, V.P., 1990. *Carbonate Sedimentology*. Blackwell Publishing, Oxford (462 pp.).
- Webb, P.-N., Strong, C.P., 2006. Foraminiferal biostratigraphy and palaeoecology in Upper Oligocene–Lower Miocene glacial marine sequences 9, 10, and 11, CRP-2/2A drill hole, Victoria Land Basin, Antarctica. *Palaeogeography, Palaeoclimatology, Palaeoecology* 231, 71–100.
- Wise, W.S., Nokleberg, W.J., Kokinos, M., 1969. Clinoptilolite and ferrierite from Agoura, California. *American Mineralogist* 54, 887–895.
- Zachos, J., Pagani, H., Sloan, L., Thomas, E., Billups, K., 2001. Trends, rhythms, and aberrations in global climate: 65 Ma to present. *Science* 292, 686–693.